Biomaterials 303 (2023) 122398

Contents lists available at ScienceDirect

Biomaterials

journal homepage: www.elsevier.com/locate/biomaterials

Development of miR-26a-activated scaffold to promote healing of critical-sized bone defects through angiogenic and osteogenic mechanisms

Joanna M. Sadowska [a,1], Monika Ziminska [b,1], Cole Ferreira [c,1], Austyn Matheson [a], Auden Balouch [c], Jasmine Bogle [c], Samantha Wojda [c], John Redmond [d], Ahmed Elkashif [b], Nicholas Dunne [b,d,e,f,g], Helen O. McCarthy [b], Seth Donahue [c], Fergal J. O'Brien [a,c,f,*]

[a] Tissue Engineering Research Group, Dept. of Anatomy and Regenerative Medicine, Royal College of Surgeons in Ireland (RCSI) University of Medicine and Health Sciences, Dublin, Ireland
[b] School of Pharmacy, Queen's University Belfast, Belfast, United Kingdom
[c] Department of Biomedical Engineering, University of Massachusetts Amherst, USA
[d] Advanced Materials and Bioengineering Research Centre (AMBER), RCSI and TCD, Dublin, Ireland
[e] Advanced Manufacturing Research Centre (I-Form), School of Mechanical and Manufacturing Engineering, Dublin City University, Dublin, Ireland
[f] Trinity Centre for Biomedical Engineering, Trinity College Dublin (TCD), Dublin, Ireland
[g] School of Mechanical and Manufacturing Engineering, Dublin City University, Dublin, Ireland

ABSTRACT

Very large bone defects significantly diminish the vascular, blood, and nutrient supply to the injured site, reducing the bone's ability to self-regenerate and complicating treatment. Delivering nanomedicines from biomaterial scaffolds that induce host cells to produce bone-healing proteins is emerging as an appealing solution for treating these challenging defects. In this context, microRNA-26a mimics (miR-26a) are particularly interesting as they target the two most relevant processes in bone regeneration-angiogenesis and osteogenesis. However, the main limitation of microRNAs is their poor stability and issues with cytosolic delivery. Thus, utilising a collagen-nanohydroxyapatite (coll-nHA) scaffold in combination with cell-penetrating peptide (RALA) nanoparticles, we aimed to develop an effective system to deliver miR-26a nanoparticles to regenerate bone defects *in vivo*. The microRNA-26a complexed RALA nanoparticles, which showed the highest transfection efficiency, were incorporated into collagen-nanohydroxyapatite scaffolds and *in vitro* assessment demonstrated the miR-26a-activated scaffolds effectively transfected human mesenchymal stem cells (hMSCs) resulting in enhanced production of vascular endothelial growth factor, increased alkaline phosphatase activity, and greater mineralisation. After implantation in critical-sized rat calvarial defects, micro CT and histomorphological analysis revealed that the miR-26a-activated scaffolds improved bone repair *in vivo*, producing new bone of superior quality, which was highly mineralised and vascularised compared to a miR-free scaffold. This innovative combination of osteogenic collagen-nanohydroxyapatite scaffolds with multifunctional microRNA-26a complexed nanoparticles provides an effective carrier delivering nanoparticles locally with high efficacy and minimal off-target effects and demonstrates the potential of targeting osteogenic-angiogenic coupling using scaffold-based nanomedicine delivery as a new "off-the-shelf" product capable of healing complex bone injuries.

1. Introduction

Large bone defects incurred through disease and trauma considerably diminish the supply of blood, nutrients, and vascularisation to the affected area, thereby impeding the bone's self-regeneration capacity and often leading to delayed or unsuccessful tissue union [1,2]. The treatment of these defects still remains a challenge to clinicians. Over the years, autografts harvested from the patient's iliac crest have become the gold standard, as they contain viable host cells and bone matrix proteins that enhance both osteoconductive and osteoinductive properties. Nonetheless, they are associated with limited availability, high donor-side morbidity, and the need for two surgical interventions, increasing the risk of complications [3,4]. This, combined with the growing demand for bone grafting, has led modern biomaterials science to focus on designing synthetic materials that not only provide structural support but also actively participate in the bone healing process by stimulating host cells to deposit bone matrix [5]. This can be achieved by delivering nanomedicines and therapeutics to induce the host cells to produce bone-healing proteins by themselves [6,7].

In current clinical practice, the delivery of growth factors, such as

---

[*] Corresponding author. Tissue Engineering Research Group, Dept. of Anatomy and Regenerative Medicine, Royal College of Surgeons in Ireland (RCSI) University of Medicine and Health Sciences, Dublin, Ireland

E-mail address: fjobrien@rcsi.ie (F.J. O'Brien).

[1] equal contribution.

https://doi.org/10.1016/j.biomaterials.2023.122398
Received 8 June 2023; Received in revised form 19 October 2023; Accepted 10 November 2023

recombinant bone morphogenetic protein-2 (BMP-2), is commonly employed for bone repair. However, growth factors have inherent limitations, including uncontrolled release, short half-life, ectopic bone formation, and targeting only a single pathway in the complex signalling cascade of bone healing [8–10]. As a result, there is growing interest in the intracellular delivery of nucleic acids, including microRNAs (miRNAs), which exhibit multifunctionality by targeting multiple genes and pathways MicroRNAs are small non-coding RNA molecules that naturally occur within cells and regulate gene expression at the post-transcriptional level [11]. Synthetic therapeutic microRNAs, including miR mimics and antagomiRs, can either mimic or inhibit gene function, thereby leading to the overexpression or downregulation of specific targets and proteins [12,13]. The delivery of microRNAs offers several advantages over other nanotherapeutics. Unlike recombinant proteins such as BMP-2, microRNAs do not require supraphysiological dosages, reducing the risk of aberrant effects [14,15]. In addition, the lower molecular weight is easier to complex and deliver to the cytoplasm compared to plasmid DNA which requires nuclear transcription before cytoplasmic translation.

A range of microRNAs have been identified as key regulators of bone regeneration. For example, miR-133a [16], miR-16 [17] or miR-138 [18] have been reported to positively influence osteogenesis. At the same time, miR-126 [19] or miR-210 [20] have been shown to induce angiogenesis of endothelial or mesenchymal stem cells [21] by stimulating the expression of vascular endothelial growth factors (VEGF) or hypoxia-inducible factors (HIF). Among the numerous microRNAs involved in essential processes, microRNA-26a (miR-26a) stands out as particularly intriguing in the context of bone, as it plays a role in both angiogenesis and osteogenesis, making it a promising candidate for bone tissue applications. Specifically, miR-26a mimics have been found to stimulate multiple osteogenic pathways, leading to the overexpression of relevant proteins such as Runx2 and osteocalcin [22–26]. Furthermore, miR-26a mimics promote osteogenic differentiation and mineralisation of MSCs [27] while inhibiting osteoclastogenesis [28], underscoring their role in maintaining bone homeostasis. Notably, miR-26a has been shown to induce the overexpression of VEGF [26], a potent angiogenic molecule, highlighting its potential involvement in the angiogenic-osteogenic coupling process in bone regeneration.

While microRNAs potentially offer cutting-edge solutions in tissue engineering and regenerative medicine, the major challenges lie in protecting miRs against enzymatic degradation while allowing for steady and controlled release of genetic cargo to the host cell. Our research group has been exploring the combination of scaffolds and non-viral vectors for the delivery of a multitude of nucleic acids to tissue-specific applications for the last decade [29]. Gene-activated scaffold systems leverage the structural support and bioactive environment of scaffolds and the safe protective role of non-viral vectors to deliver therapeutics locally at the clinical site, reducing doses and administration frequency, and potentially enhancing efficacy compared to systemic administration [29]. Specifically in relation to bone repair, our collagen-hydroxyapatite scaffold platforms have demonstrated significant potential in healing bone defects in small and large animal models [30–32] Moreover, they have proven to be effective systems for the controlled delivery of nucleic acids, including plasmid BMP-2 [33], plasmid VEGF [34] and microRNAs [16,17].

In this study, we utilise the RALA peptide as a non-viral delivery vector, known for its ability to effectively complex anionic cargoes [35, 36] thus protecting the cargo from enzymatic degradation and ensuring its delivery into the cellular cytosol. This approach was driven by the proven *in vivo* efficacy and safety of the RALA peptide [37,38]. The objective of the study was thus to develop a highly efficient non-viral gene-activated scaffold capable of simultaneously promoting blood vessel ingrowth and bone formation for the repair of large bone defects by delivering miR-26a mimics protected with RALA peptide. To achieve this, our study encompassed specific aims: 1) optimising miR-26a-RALA nanoparticles and assessing their osteogenic potential in 2D cell cultures using hMSCs, 2) developing a miR-26a-activated scaffold and evaluating its loading efficiency, transfection efficiency, release capability, as well as its effects on the angiogenic and osteogenic potential of MSCs, and 3) evaluating the ability of miR-26a-activated scaffolds to regenerate critical-sized calvarial defects *in vivo*.

2. Materials and methods

2.1. Development of miR-26a nanoparticles

The miRIDIAN microRNA hsa-miR-26a-5p mimic (miR-26a) and scrambled mimic negative control (scr miR) (Dharmacon, UK) were combined with RALA peptide (Biomatik, US) at N:P ratios ranging from 1 to 10. This formulation allowed for the spontaneous formation of complexes within 30 min, following the methodology outlined in McCarthy et al., [35]. To enable fluorescent tracking of the microRNA nanoparticles, miR-26a was labelled with Cy5 through covalent binding, utilising the Label IT® siRNA Tracker Intracellular Localisation Kit (Cambridge Bioscience, UK) according to the manufacturer's instructions. Subsequently, the labelled miR-26a (miR-26a-Cy5) was complexed with RALA at an N:P ratio of 8, as previously described. All nanocomplexes containing genetic cargoes were then lyophilised in 2 mL vials using a programmable AdVantage Pro freeze dryer (SP Scientific, USA), with trehalose employed as a cryoprotectant.

2.2. Physicochemical characterisation of miR-26 nanoparticles

2.2.1. Size, zeta-potential and morphology

The optimal N:P ratio of miR-26a nanoparticles was determined through various characterisation techniques. The mean hydrodynamic size of freshly prepared and reconstituted nanoparticles containing 0.5 μg of microRNA in water was measured using Dynamic Light Scattering on a Malvern Nano ZS instrument (Malvern Instruments, UK). The zeta potential of the nanoparticles in each sample was determined using Laser Doppler Velocimetry on the same Malvern Nano ZS system. All measurements were conducted at room temperature.

The morphology of miR-26a nanoparticles was examined using transmission electron microscopy. A 10 μL sample was placed on a copper-carbon mesh grid (TAAB Laboratories, UK) and allowed to sit for 3 min. The grid was then dried overnight and stained with UranyLess (EMS, USA) for 3 min at room temperature. Imaging of the grids was performed using a JEM-1400 Plus Transmission Electron Microscope (JEOL, USA) operating at an accelerating voltage of 80 kV.

2.2.2. Complexation efficiency and stability

The complexation efficacy of genetic cargo by the RALA peptide was assessed using spectrophotometry and ion exchange chromatography. To evaluate complexation efficiency, 0.5 μg of microRNA was formulated at N:P ratios ranging from 0 to 20, and Quant-IT™ microRNA reagent (Thermo Fisher Scientific, UK) was employed for quantification. Measurements were conducted on an OmniStar plate reader (BioTek Instruments Inc., UK) according to the manufacturer's instructions, with complexation efficiency calculated relative to a naked miR control.

Confirmation of miRNA complexation by the RALA peptide was performed using Ion Exchange Chromatography (IEC). A 0.5 g portion of SP-Sephadex, an Ion Exchange Media (Sigma-Aldrich, SPC25120, GER), was incubated overnight at room temperature in 10 mL of 1 M molecular biology grade NaCl (Sigma-Aldrich, Germany) to facilitate column swelling. The supernatant was removed, and the resin was washed thrice with 10 mL of Ultrapure water to eliminate any residual ionic solvent. Subsequently, 20 μL of naked miR-26a or miR-26a-RALA nanoparticles, with a concentration of ≥20 mg/mL, was loaded into the column and eluted with 3 mL of ultrapure water. The collected fractions were analysed using UV–Vis Spectroscopy.

To assess the impact of temperature on nanoparticle stability, miR-26a complexed with RALA at an N:P ratio of 8 was subjected to a temperature range of 4–60 °C. The stability over time was also assessed by incubating the nanoparticles at 37 °C up to 28 days. Size analysis was performed using the Nano ZS DTS software (Malvern Instruments, UK).

2.3. Effect of miR-26a nanoparticles on human mesenchymal stem cells in 2D culture

2.3.1. Cell transfection

To ensure effective delivery of miR-26a into hMSCs (Lonza) derived from iliac crest bone marrow aspirates, cell transfection was evaluated. HMSCs were seeded at a density of 20,000 cells per well in a 24-well plate (VWR, UK) and cultured for 24 h in low-glucose DMEM supplemented with 10 % foetal bovine serum and 1 % penicillin/streptomycin (all from Sigma-Aldrich, UK).

For transfection, the cells were conditioned for 2 h in Opti-MEM serum-free medium (Gibco, UK), followed by the addition of 0.5 μg of miR-26a. After 5 h, the transfection medium was replaced with a growth medium. On day 3, complete osteogenic media containing 50 μg/mL ascorbic acid-2-phosphate, 10 nM β-glycerophosphate, and 100 nM dexamethasone (all from Sigma-Aldrich, UK) were added to induce osteogenic differentiation.

The upregulation of miR-26a in hMSCs was assessed using quantitative Real-Time PCR (qRT-PCR). On days 1, 3, and 7 post-transfection, RNA was extracted from hMSCs using RNeasy kits (Qiagen, UK), and reactions were prepared for each set of probes following the manufacturer's protocols (TaqMan Small RNA assay, Invitrogen, UK). qRT-PCR was performed using a Lightcycler 480 II (Roche, UK), and the ΔΔCT method was used to determine the fold change in the expression of genes of interest.

2.3.2. Metabolic activity and viability

To confirm that miR-26a nanoparticles do not exhibit cytotoxic effects on cells, cells were seeded in 24-well plates (VWR, UK) at a density of 15,000 cells per well and transfected with the nanoparticles. The cells were then incubated at 37 °C under 5 % CO_2 for up to 21 days.

To evaluate cell viability, the metabolic activity of the cells was measured using the AlamarBlue Cell Viability assay (ThermoFisher, UK) on days 7, 14, and 21 post-transfection. The absorbance was measured at 560/590 nm using an OmniStar plate reader (BioTek Instruments Inc., UK).

In addition, the DNA content of the cells was quantified to further confirm cell viability. On days 3, 7, 14, and 21 post-transfection, cells were lysed using Triton X-100 (Cambridge Biosciences, UK). The DNA content was quantified using a Quant-iT PicoGreen dsDNA kit (Invitrogen, UK), and fluorescence was measured at 480/520 nm using an OmniStar plate reader (BioTek Instruments Inc., UK). This allowed for the assessment of cell proliferation and viability over time.

2.3.3. Intracellular delivery and internalisation of miR-26a nanoparticles

To demonstrate the efficient delivery of genetic cargoes to the cytosol of cells, both microscopic and flow cytometry techniques were employed using a murine fibroblast cell line (NCTC-L929) and primary cells (hMSCs). NCTC-L929 cells were seeded at a density of 15,000 cells per well in a 96-well plate and transfected with miR-Cy5 as previously described [39].

Briefly, the transfected cells were fixed and permeabilised using a solution containing 4 % formaldehyde and 0.1 % Triton-X (Sigma, UK) for 30 min. Subsequently, the cells were stained with Fluorescein Phalloidin (Invitrogen, UK) at room temperature for 15 min to visualise F-actin. The stained cells were mounted onto microscope slides using Fluoroshield mounting medium containing a DAPI nuclear stain (Life Technologies, UK). Imaging of the cells was performed using a TSC SP5-Leica Microsystems confocal microscope (Leica, UK) and visualised using LAS AF Lite Software (Leica, UK).

To investigate the internalisation of nanoparticles by hMSCs, cells were transfected with miR-Cy5 at N:P ratios of 6, 8, and 10 in a 96-well plate with a seeding density of 15,000 cells. After 24 h, the hMSCs were trypsinised, resuspended in PBS, and analysed using a fluorescence-activated cell sorting (FACS) Calibur system (BD Biosciences, UK). The acquired data were analysed using BD CellQuest™ Pro software. Fluorescence intensity was evaluated with a 0.5 % gating strategy to determine the efficiency of nanoparticle uptake by the cells.

2.3.4. Effect of miR-26a nanoparticles on human mesenchymal stem cell-mediated osteogenesis in 2D

The therapeutic effects of the selected cargo on the osteogenesis of hMSCs were assessed by quantifying alkaline phosphatase (ALP) activity and calcium content. ALP activity was measured at days 3, 7, and 14 post-transfection using a SensoLyte® pNPP AL assay kit following the manufacturer's instructions. The absorbance was recorded at 405 nm using a suitable spectrophotometer.

To determine the calcium content, samples were collected at days 7, 14, and 21 post-transfection. The calcium content was quantified using a Calcium Liquicolor kit (Stanbio Inc., USA). The absorbance was measured at 540 nm using the OmniStar plate reader (BioTek Instruments Inc., UK).

2.4. miR-26a-scaffold fabrication

Collagen-nanohydroxyapatite (coll-nHA) scaffolds (10 mm in diameter, 4 mm in height) were prepared as previously described [16,17,40]. Briefly, the collagen type I (Southern Light Biomaterials, New Zealand) was dissolved in 0.5 M of acetic acid at 5 mg/mL and the in-house produced nHA particles were homogenously added to the slurry at a 1:1 collagen-to-nHA weight ratio. The scaffolds were then lyophilised in an Advantage Pro Benchtop Freeze Dryer (SP Industries) at a −40 °C final freezing temperature. The coll-nHA scaffolds were sterilised using a dehydrothermal (DHT) treatment, cross-linked for 2 h in 6 mM N-(3-Dimethylaminopropyl)-N′-ethyl carbodiimide hydrochloride (EDAC, Sigma-Aldrich, Ireland) and 5.5 mM N-hydroxysuccinimide (NHS, Sigma Aldrich) in dH_2O and rinsed trice with Dulbecco's Phosphate Buffered Saline. Coll-nHA scaffolds were then soak-loaded with either 1 or 3 μg of miR-26a nanoparticles. This soak-loading approach improves the release kinetic, allowing cells easier access to the nanoparticles, as they are not covalently attached to the surface.

2.5. Microstructure of miR-26a activated-scaffold and release profiles

To confirm that the incorporation of miR-26a nanoparticles does not affect scaffold microstructure and architecture previously optimised for bone regeneration, the scaffolds were assessed under a scanning electron microscope. MiR-free scaffolds and miR-26-activated scaffolds at 1 and 3 μg dosage were mounted onto metallic studs and sputtered using a gold/palladium alloy, a Cressington 108 auto sputter coater (Cressington Scientific Instruments, UK). The microstructure of the scaffolds was assessed using a Zeiss Ultra Plus scanning electron microscope (Zeiss, Germany) at 5 kV. To confirm the equal distribution of miR-26a nanoparticles within the structure, the cross-sections (4 mm of height) containing fluorescently labelled miR-Cy5 were visualised using a Carl Zeiss LSM 710. Images were prepared in FIJI.

To assess loading efficiency and release profiles of miR-26a, the scaffolds were placed in 24-well plates, and 30 μL of miR-26a NPs were added per scaffold side and incubated for 1 h at 37 °C to ensure proper penetration. Then, the scaffolds were transferred to the new well plate, and the release study was performed at 37 °C in static conditions using 2 mL of Optimem. The release study was performed at 37 °C in static conditions. The 200 μL of media was recovered at specific time points, and fresh 200 μL was added per well. The 200 μL were incubated with 50 μL of Proteinase K (1 mg/mL) for 90 min at 37 °C to dissociate NPs and release microRNA. The amount of the microRNA was quantified using the Ribogreen assay (Thermofisher, Ireland) following the manufacturer's instructions.

2.6. Effect of scaffold-mediated miR-26a transfection on human MSC-mediated angiogenesis and osteogenesis in vitro

Bone marrow aspirates were purchased in Lonza to obtain hMSCs following stem phenotype analysis. The hMSCs were expanded in low-glucose DMEM. The cells up to passage 5 were used for the experiments. For transfections, the coll-nHA scaffolds were loaded with either 1 or 3 μg of miR-26a nanoparticles in 50 μL and incubated with 3×10^5 human mesenchymal stem cells (hMSCs) for 4 h in Optimem. After that time, the medium was replaced with low-glucose DMEM. The osteogenic media was administered on day 1 post-transfection.

Expression of miR-26a was determined at day 3 post-transfection using Real-Time Polymerase Chain Reaction (qRT-PCR) and following the procedures described in section 2.3.1.

2.6.1. Analysis of miR-26a-activated scaffolds on hMSCs-mediated osteogenesis

To determine if miR-26a-activated scaffolds stimulate osteogenesis in hMSCs, alkaline phosphatase (ALP), an early osteogenic marker, and calcium were measured on days 14 and 28, respectively. The osteogenic markers were measured at day 7 and detected through qRT-PCR. The detailed protocols can be found in Sections 2.3.1 and 2.3.4.

Additionally, scaffold mineralisation was assessed histologically and using elemental analysis after 28 days in cell culture. For histological staining, the scaffolds were fixed with 10 % of formalin, processed at 7 μm serial sections and stained with 2 % Alizarin red to determine calcium deposits. The elemental analysis was performed using the EDX system within the Zeiss LS 15. The scaffolds were dehydrated using ascending alcohol series, sputter coated with gold particles (Scancoat Six, BOC Edwards, United Kingdom) and imaged at an accelerating voltage of 5 kV.

2.6.2. Analysis of miR-26a-activated scaffolds on hMSCs-mediated angiogenesis

The angiogenic effects of miR-26a-scaffolds on hMSCs were evaluated through quantification of Vascular Endothelial Growth Factor (VEGF), a target of miR-26a, by qRT-PCR and Enzyme-Linked Immunosorbent Assay (ELISA). The angiogenic markers were measured at day 7 and detected through qRT-PCR as described in Section 2.3.1. The levels of VEGF protein in hMSCs transfected with miR-26a were analysed on day 14 following the manufacturer's instructions (R&D Systems, UK). The absorbance of each sample was read at 450 nm using a Varioskan Flash multimode plate reader (Fisher Scientific, Ireland).

2.7. Effect of cell culture on mechanical properties of miR-activated scaffolds

The mechanical properties of the miR-free and miR-scaffolds were evaluated through unconfined compression testing after day 28 in cell culture. A total of six samples per group were tested. In order to establish reference values, three control groups were included: cell-free scaffold at day 0, cell-free scaffold at day 28, and cell-seeded scaffold at day 28.

Unconfined compression testing was performed using the Z050 Zwick/Roell mechanical testing machine (Zwick GmbH & Co., Ulm, Germany) equipped with a 5 N load cell. To maintain scaffold hydration during testing, a custom water bath held at 37 °C was utilised. The testing protocol involved applying a constant deformation rate of 10 % strain per min. The elastic modulus, a measure of the scaffold's stiffness, was calculated by determining the slope of the stress/strain curve within the linear 2–5% deformation range. This region was selected as it represents the linear portion of the curve where the scaffold exhibits elastic behaviour.

2.8. Analysis of the efficacy of miR-26a-activated scaffolds to accelerate bone healing in a calvarial defect in rats

2.8.1. Surgical procedure

All housing and *in vivo* experimental procedures were performed in accordance with protocol #2466, approved by the Institutional Animal Care and Use Committee (IACUC) of the University of Massachusetts Amherst. Sixteen Male Wistar Rats (11 weeks old, 340–400 g) were used in this experiment. The animals were kept in the temperature-controlled University of Massachusetts Amherst animal care facility and had *ad libitum* access to food and water, as well as a standard day/night cycle. The animals were randomly divided evenly into 2 treatment groups. Each group received a collagen-hydroxyapatite scaffold soak-loaded with either pure water (miR-free scaffold) or 1 μg of miR-26a nanoparticles. The animals were administered 0.05 mg/kg of buprenorphine hydrochloride as a pre-emptive analgesic at least 30 min prior to surgery. The rats were anaesthetised via isoflurane inhalation (2.5%–3.5 %) and then administered cefazolin (20 mg/kg) as a prophylactic antibiotic and sterile saline (5 mL/kg) to account for fluid losses during surgery. After anaesthesia, the calvaria was exposed via a midline incision and lateral contraction of the skin and periosteum. A dental drill in combination with a 7-mm trephine operating at 1500 rpm was used to create a 7-mm unilateral circular trans osseous defect. Precision was used so as to not damage the underlying dura matter, which can impede the healing process. A surgical elevator and forceps were used to elevate the excised disk of bone, creating the defect region. The soak-loaded collagen-hydroxyapatite scaffold was then gently inserted into the defect. Following treatment administration, the periosteum and skin were reflected over the defect site and closed with 4-0 monofilament absorbable sutures and wound clips. Post-surgery, the animals were allowed to recover and received post-hoc doses of buprenorphine hydrochloride (0.05 mg/kg) at timepoints of 12-, 24-, and 36 h. Animals were weighed and monitored for distress for 8 days following the procedure. Due to complications, one animal was lost from the experimental group. All surviving animals experienced no signs of implant rejections or inflammatory reactions.

2.8.2. Micro-computed tomography

Micro-Computed Tomography (μCT) was performed *in vivo* 4- and 8 weeks post-surgery. Animals were anaesthetised using isoflurane inhalation (2.5%–3.5 %) and placed within a cylindrical cassette inside the μCT scanner (Bruker Skyscan 1276). Anaesthesia was maintained via a nose cone throughout the entire scan. Animals were scanned with a voxel size of 40 μm and a 1 mm aluminium filter. The x-ray tube voltage was 60 kV, the current was 125 μA, and the exposure time was 539 ms. Images were collected every 0.8° using a 360° rotation around the sample. Three-dimensional image reconstructions were performed using NRecon (Bruker). All reconstructions were done with the same dynamic range of 0–0.052639. A universal beam hardening of 30 %, a Gaussian smoothing of 2, and a ring artefact correction of 10 were used on each set of images. To ensure that the region of interest (ROI) is kept in the same location, the scans from weeks 4 and 8 were aligned using DataViewer's 3D registration. A threshold of 137–255 on a scale of 0–255 was used to determine mineralised bone tissue (>0.644 g HA/cm^3). The samples percent filled (%), Bone Volume (BV) (mm^3), Bone Mineral Density (BMD) (g/cm^3), and Tissue Mineral Density (TMD) (g/cm^3) were quantified. Per cent filled is defined as the bone area over the total area of a 2D projection of a top-down view of the defect. BV is the volume of bone that was successfully regenerated in the defect region. BMD is the average mineral density of the entire volume, while the TMD is the average mineral density excluding soft tissue.

2.8.3. Histomorphometry

Histomorphometric analyses were used to further determine bone growth and structure within the defect region. Following week 8 μCT scans, the rats were anaesthetised using 2.5 %–3.5 % isoflurane and euthanatised via intracardiac exsanguination. Skulls were removed using a high speed blade, and the calvarial explants were fixed in 10 % formalin for 72 h, stored in 70 % ethanol, decalcified overnight in rapid-acting formic acid and embedded in paraffin wax blocks. Sections (5 μm thick) were cut from the middle of the defect, deparaffinised, and mounted on slides. Sections were stained using an H&E method and imaged with a Zeiss Stereo Discovery.V20. Several samples were lost during processing resulting in n = 7 for the control, and n = 5 for the experimental group. Bioquant image analysis software was used to quantify the defect width and bone area. The defect width was defined as the shortest distance between the bone from the medial side of the defect to the lateral side. Only widths greater than 25 μm were quantified to avoid misidentifying artefacts or soft tissue gaps as defects. The bone area was quantified using a region of interest that was 6 mm in width and the height of the native skull. To evaluate the effect of scaffolds on angiogenesis, the histological samples were graded from 1 to 3 with regard to the presence of blood vessels in the defect space. Blood vessels were recognised as erythrocytes encapsulated by a thin layer of connective tissue. A score of 1 indicates a low population of blood vessels, and a score of 3 indicates a high and dense population of blood vessels throughout the defect space. All samples were graded relative to each other.

2.9. *Statistical analysis*

All statistical analyses were conducted using GraphPad Prism software. The data presented in the graphs are expressed as mean ± standard error of the mean (SEM) (n = 3 and n = 8 for the *in vitro* and *in vivo* data, respectively) unless stated otherwise in the figure captions. Normality was assessed using the Shapiro-Wilk test, and any outliers were identified and excluded using Grubbs analysis. Statistical differences between groups were assessed using either the Student's t-test or one-way analysis of variance (ANOVA) followed by Tukey's post hoc test for multiple comparisons. The significance level for all tests was set at $p < 0.05$.

3. Results

3.1. *The complexation with RALA peptide led to the development of microRNA-26a nanoparticles with superior transfection efficiencies*

The mean hydrodynamic size and zeta potential of miR-26a nanoparticles complexed with RALA peptide were evaluated at various N:P ratios, both before and after lyophilisation, to determine the optimal N:P ratio for intracellular delivery and to assess the impact of lyophilisation on the nanoparticles' physicochemical properties. N:P ratios exceeding 2 resulted in particles smaller than 100 nm with a positive charge (Fig. 1A). The lyophilisation process had no adverse effect on the nanoparticles' characteristics, as they maintained suitable properties. Among the tested ratios, N:P 8 was identified as the optimal N:P ratio for subsequent osteogenic studies. Before lyophilisation, the particles at N:P 8 exhibited a z-average size of 133.9 nm, which decreased to 84.77 nm after lyophilisation, with polydispersity indices (PdIs) of 0.33 and 0.276, respectively (Fig. 1B). Transmission electron microscopy (TEM) imaging confirmed the uniformity and morphology of the nanoparticles (Fig. 1C).

The complexation efficiency of RALA was assessed using a Quant-iT™ PicoGreen™ assay, which measured the remaining concentration of nucleic acid in the solution after adding the RALA peptide. Complexation efficiencies exceeding 80 % were achieved at N:P ratios higher than 6. At the optimal N:P ratio of 8, the complexation efficiency was 81.8 % for fresh particles and 83.1 % for lyophilised particles. Furthermore, ion exchange chromatography (IEC) analysis confirmed nucleic acid retention by RALA at a rate of over 99 % (Fig. 1E).

The stability of miR-26a nanoparticles complexed with RALA was assessed over a temperature range of 4–60 °C. The nanoparticles

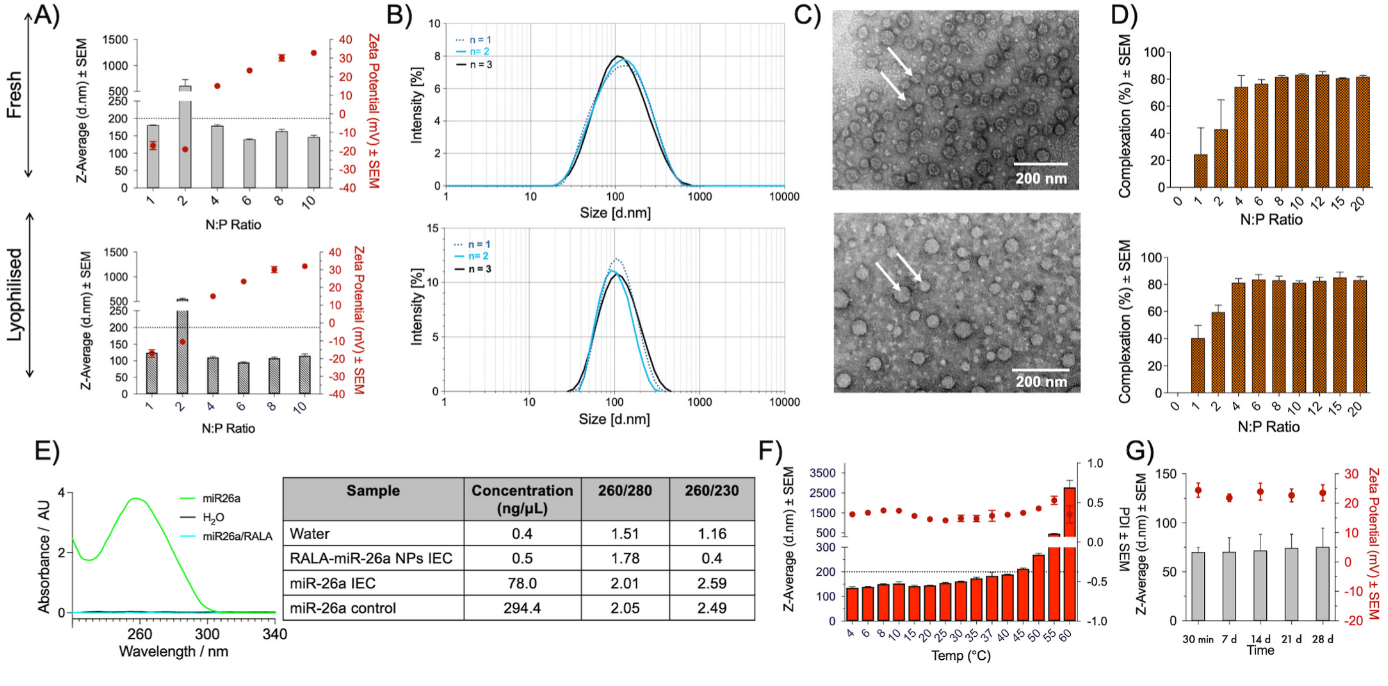

Sample	Concentration (ng/μL)	260/280	260/230
Water	0.4	1.51	1.16
RALA-miR-26a NPs IEC	0.5	1.78	0.4
miR-26a IEC	78.0	2.01	2.59
miR-26a control	294.4	2.05	2.49

Fig. 1. Physiochemical characterisation of fresh (top) and lyophilised (bottom) miR-26a-RALA showed that properties depend on N:P ratio. A) Zeta potential of miR-26a nanoparticles increased with N:P ratio. Hydrodynamic size showed similar values for nanoparticles with N:P ratio >2. **B)** The miR-26a nanoparticles showed monomodal size distribution with Z-Average and Polydispersity Index (PdI) smaller for lyophilised nanoparticles. **C)** The transmission electron microscopy (TEM) confirmed the effective formation of complexes showing that nanoparticles were spherical in shape. **D)** Both fresh and lyophilised miR-26a nanoparticles were complexed effectively with RALA peptide for N:P ratios equal or higher than 4. **E)** This was confirmed through Ion Exchange Chromatography (IEC), where no free miR-26a was observed when miR-26a-RALA nanoparticles were run through the column. **F)** The lyophilised miR-26a-RALA nanoparticles at N:P 8 exhibited stable Z-Average and PdI at the relevant range of temperatures (4–37 °C) and **G)** over 28 days at 37 °C.

exhibited stability under various temperatures, maintaining a z-average size of less than 200 nm up to 40 °C (Fig. 1F). The nanoparticles were also stable over 28 days when incubated at 37 °C (Fig. 1G). These findings indicate that the nanoparticles are capable of retaining their physicochemical characteristics under physiological temperatures.

3.2. The effective transfection of human mesenchymal stem cells (hMSCs) in 2D with miR-26a NPs led to enhanced osteogenesis

The cytotoxicity of miR-26a nanoparticles on hMSCs was evaluated over 21 days using the alamarBlue assay. The metabolic activity of cells was measured at days 7, 14, and 21 post-transfection, and no cytotoxic effects were observed with either miR-26a nanoparticles or scramble (scr) control mimics (Fig. 2A). This finding was further supported by measuring the DNA content of cells from day 3–21 post-transfection, which demonstrated a steady increase over the 21-day period with no significant difference between the untreated control and miR-26a groups (Fig. 2B).

To investigate the ability of miR-26a nanoparticles to traverse the cell membrane and be internalised, confocal microscopy using Cy5-labelled nanoparticles was employed. At 4 h post-transfection, nanoparticles in the cytosol and nucleus of NCTC-929 cells were clearly observed (Fig. 2C, white arrows). Orthogonal sectioning further confirmed the localisation of nanoparticles within the cytoskeleton. Flow cytometric analysis revealed high percentages of internalisation for all tested N:P ratios (Fig. 2D), with N:P 8 exhibiting the highest internalisation percentage (87.4 %), thus supporting its selection as the optimal N:P ratio. Moreover, all N:P ratios demonstrated significantly increased fluorescence intensity, with N:P 8 displaying the highest fluorescence.

To assess the functionality of the nanoparticles, hMSCs were transfected with 0.5 μg of miRNA, followed by qRT-PCR analysis of miR-26a mRNA levels. Significant upregulation of miR-26a was observed from day 1 post-transfection, and this upregulation was sustained until day 7 (Fig. 2F). Notably, N:P 8 resulted in the highest levels of miR-26a, exhibiting over a 2500-fold increase on day 1, 1495-fold increase on day 2, and a 558-fold increase on day 7. Collectively, these results demonstrate the ability of miR-26a nanoparticles to significantly upregulate miR-26a in hMSCs with minimal cytotoxic effects over 7 days.

To evaluate the osteogenic potential of miR-26a nanoparticles, hMSCs were cultured in osteogenic media, providing the necessary nutrients and growth factors for osteodifferentiation. Calcium deposition, an indicator of matrix maturation, was quantified on day 7, 14, and 21 post-transfection (Fig. 3A, Supp Fig. 1A). Notably, hMSCs transfected with miR-26a exhibited significantly increased calcium deposition at both day 14 and 21, with a 27 % increase compared to the control group. The activity of ALP, an early marker of bone mineralisation, was measured at days 3, 7, and 14 following transfection. Transfection with miR-26a resulted in a significant enhancement of ALP activity at days 3 and 7 compared to the untransfected control. Furthermore, there was a sustained increase in ALP activity at day 14 (Fig. 3B, Supp Fig. 1B). These findings are consistent with ALP's role as an early indicator of bone formation, promoting the reduction of extracellular pyrophosphate and facilitating matrix formation and mineralisation.

3.3. Collagen-nanohydroxyapatite scaffolds present high loading efficiency and controlled release of miR-26a nanoparticles

The miR-26a NPs were effectively incorporated into collagen nano-hydroxyapatite (coll-nHA) scaffolds at two different concentrations – 1 μg and 3 μg. The effective incorporation of miR-26a NPs was demonstrated by high loading efficiency of over 96 % (Fig. 4A). Furthermore, the SEM images showed that coll-nHA scaffolds were functionalised with miR-26a NPs and that soak-loaded NPs were uniformly retained on the scaffold structure (Fig. 4B, white arrows). Importantly, the miR-26a-activated scaffolds showed similar architecture and microstructure compared to miR-free scaffolds, and thus, they retained optimal for bone repair physicochemical features. The CLSM images with miR-26a tagged

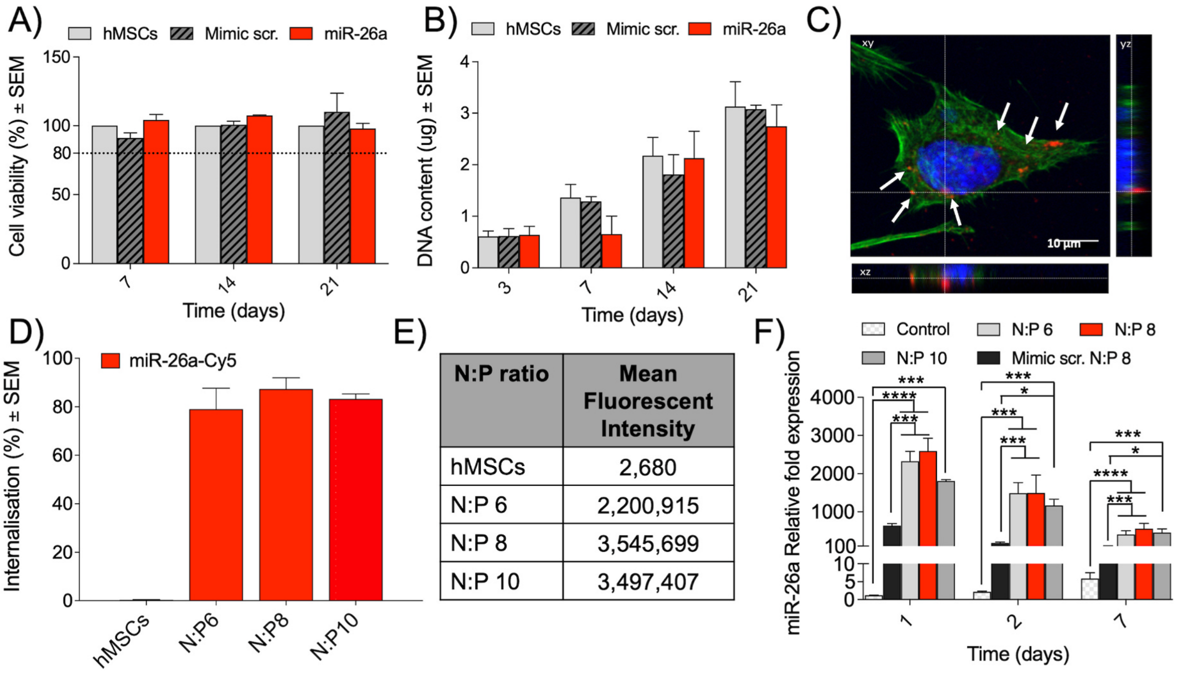

N:P ratio	Mean Fluorescent Intensity
hMSCs	2,680
N:P 6	2,200,915
N:P 8	3,545,699
N:P 10	3,497,407

Fig. 2. miR-26a and RALA complexes showed no toxic effects in 2D hMSCs culture A) The hMSCs maintained viability and **B)** increased DNA content, showing proliferative potential, while incubated with complexes. **C)** The confocal images of NCTC L-929 fibroblast cells demonstrated the effective integration of miR-26a-Cy5-RALA nanoparticles with the cellular membrane (white arrows). **D)** The effective internalisation of miR-26a nanoparticles was also confirmed using FACS and **E)** by quantifying mean fluorescent intensity within hMSCs transfected with various N:P ratios. **F)** The PCR data confirmed effective transfection with cargoes showing increased expression of miR-26a in hMSCs up to 7 d of the study. *, *** and ****$p < 0.05$, $p < 0.001$, and $p < 0.0001$, respectively. The dashed black line on graph A indicates a threshold of 80 % of viability.

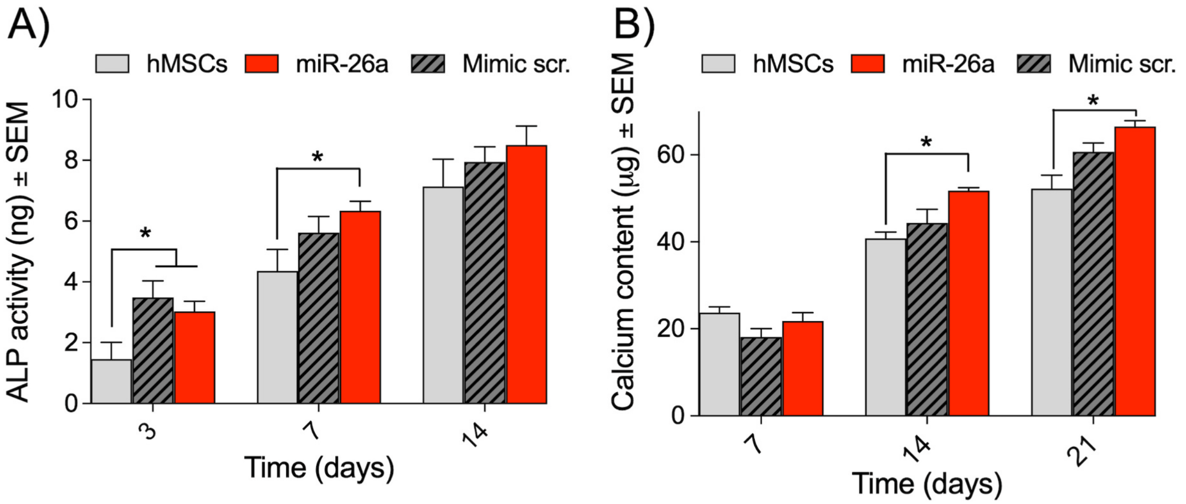

Fig. 3. miR-26a nanoparticles enhanced osteogenesis of hMSCs *in vitro*. A) hMSCs increased levels of ALP, an early osteogenic marker, and **B)** showed greater mineralisation by increasing calcium production. *$p < 0.05$.

with fluorescent Cy5 present the cross-section of the scaffolds (Fig. 4B), demonstrating that the genetic cargo was incorporated effectively within the entire thickness of the scaffolds (4 mm).

The controlled and sustained release of genetic cargo is a key factor for effective transfection. Thus, we evaluated the release profiles of miR-26a NPs within 28 days *in vitro*. The scaffolds released 211 ng ± 32 and 257 ng ± 22 during the first 24 h for 1 μg miR-26a and 3 μg miR conditions, respectively (Fig. 4C–E). This corresponds to 21 % ± 3 and 8 % ± 1 of the total incorporated cargo, respectively (Fig. 4E). The initial release was followed by the plateau phase for up to 28 days. Overall, the 1 μg miR-26a-scaffold retained 711 ng ± 34 whilst the 3 μg miR-26a-scaffold retained 2651 ng ± 56 (Fig. 4F–G), which corresponds to 73 % ± 3 and 91 % ± 4 (Fig. 4H) of a total of incorporated cargo, respectively. Overall, the results show that the scaffolds effectively incorporated miR-26a NPs, retaining most of the cargo for up to 28 days.

3.4. *Scaffold-facilitated transfection of hMSCs with miR-26a enhances osteogenic differentiation and stimulates the release of angiogenic factors*

Having confirmed the effective incorporation of and release of miR-26a NPs from the scaffolds, we next sought to determine if miR-26a-activated scaffolds are capable of effectively transfecting human mesenchymal stem cells (hMSCs) and inducing their osteogenic and angiogenic response. The expression of miR-26a was determined at day 3 post-transfection, reaching 64-fold and 84-fold for 1 μg miR-26a and 3 μg miR conditions, respectively (Fig. 5A). These values were statistically higher compared to a miR-free scaffold or scaffold containing negative control (scrambled miR, scr miR). This resulted in an increased production of alkaline phosphatase ALP, an early osteogenic marker, at day 14, being statistically significant only for scaffolds containing 3 μg of miR-26a (Fig. 5B). Additionally, the miR-26a-activated scaffolds that were brought forward for *in vivo* evaluation were screened in terms of enhancement of osteogenic genes, showing statistically higher values for SPP1, SMAD4, and POSTN compared to the miR-free scaffold. The scaffolds containing genetic cargoes showed significantly higher values of calcium at day 28 (Fig. 5D), demonstrating higher levels of mineralisation. This was also confirmed through Alizarin red staining of calcium deposits (Fig. 5E) and elemental mapping by Energy Dispersive X-Ray Analysis (Fig. 5F).

The increased mineralisation on scaffolds containing genetic cargoes led to higher compression modulus compared to acellular and miR-free scaffolds (Fig. 6A, Supp Fig. 1). The angiogenic potential of the scaffolds was then assessed by quantifying the vascular endothelial growth factor (VEGF) through rt-qPCR and ELISA. The hMSCs cultured on the 3 μg miR-26a-scaffolds showed significantly higher expression of VEGF at day 3 compared to the cells cultured on miR-free scaffolds (Fig. 6B). Similarly, the cells showed greater secretion of VEGF protein at day 14 compared to the control (Fig. 6C). The miR-26a-activated scaffolds, which were further implanted *in vivo*, also enhanced the expression of genes involved in angiogenesis, including PDGFA, PGF, TIMP1, and TAZ (Fig. 6D).

3.5. *miR-26a-scaffolds stimulate the formation of highly-mineralised and vascularised bone tissue resulting in repair of a critical-sized defect in vivo*

The final goal of the study was to determine the ability of miR-26a-activated scaffolds to heal critical-sized bone defects *in vivo*. Thus, the constructs were implanted into well-established 7 mm calvarial defect in male rats [40–42], and the bone growth was assessed over the time of 8 weeks. The μCT analysis showed limited bone repair in the miR-free scaffold (Fig. 7A). The miR-26a-scaffold induced the formation of new bone, reaching the values of 50.0 % ± 13.41 and 56.70 % ± 1 8.23 at weeks 4 and 8, respectively; this represented a 1.7-fold and 1.6-fold increase over miR-free scaffold (Fig. 7B). These results were confirmed through bone volume quantification (Fig. 7C). The implantation of the miR-26a scaffold resulted in a greater increase in bone volume compared to the miR-free scaffold reaching 1.8-fold and 1.9-fold higher values at week 4 and week 8, respectively. Importantly, the miR-26a-scaffold stimulated the formation of high-quality tissue, enhancing bone mineral density (0.30 g/cm^3 ± 0.08) compared to the miR-free scaffold (0.19 g/cm^3 ± 0.05) with this value over 55 % higher (Fig. 7D). Overall, the μCT data showed that the implantation of the miR-26a scaffold resulted in significantly higher levels of healing at the 8-week time point compared to the miR-free scaffold. The tissue mineral density remained unchanged (Fig. 7E).

This data was additionally validated through the histological evaluation of H&E explants (Fig. 7F). A newly formed bone matrix was identified by the dark pink staining. Both conditions presented well integration of the scaffolds within a defect site and high cellular infiltration. Histomorphometry was used to quantify the area of new bone within each defect of the H&E-stained sections (Fig. 7G and H). Although the results are not significant, the tendencies observed corroborate with the results shown by μCT. The miR-26a-activated scaffolds enhanced bone bridging, reducing the defect width to 28.62 mm ± 14.52, which is 0.3-fold lower compared to the miR-free scaffold (37.43 mm ± 14.64). Consequently, this resulted in the greater bone area within the defect site reaching the 1.9-fold higher value for miR-26a-scaffold (1.82 mm^2 ± 0.66) compared to miR-free condition

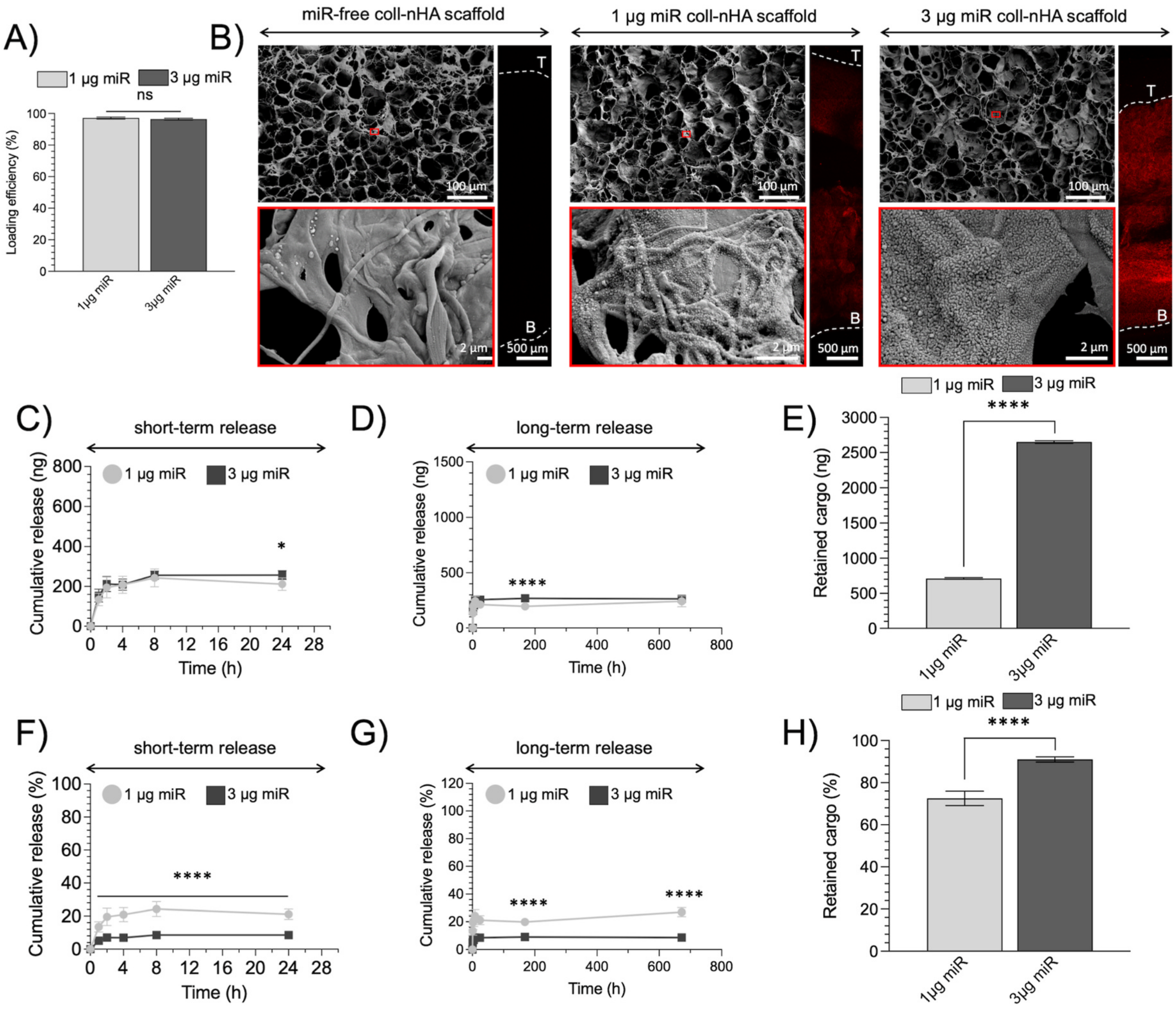

Fig. 4. The miR-26a-activated scaffolds effectively showed a high retention rate of miR-26a nanoparticles A) The scaffolds showed high loading efficacy. **B)** The miR-26a nanoparticles were homogenously distributed within the coll-nHA scaffolds without affecting their porous architecture (white arrows). The fluorescent staining of miR-26a nanoparticles with Cy5 showed that the nanoparticles penetrated the coll-nHA scaffold within the thickness. The dashed line indicates the top (T) and bottom (B) edges of the scaffold. **C) and D)** The miR-26a-activated scaffolds showed an initial partial release of the cargo of approximately 250 ng. **E)** Consequently, the coll-nHA scaffolds retained 760 ng and 2740 ng for 1 μg miR coll-nHA scaffold and 3 μg miR coll-nHA scaffold, respectively. **F) and G)** The scaffold released up to 21 % and 8 % of the initial loaded cargo within the first 24 h for 1 μg miR coll-nHA scaffold and 3 μg miR coll-nHA scaffold, respectively. **H)** The 1 μg miR coll-nHA scaffold retained up to 73 % of the cargo whilst 3 μg miR coll-nHA scaffold retained up to 91 % within the duration of the study (28 days). Ns – non-significant, * and ****$p < 0.05$ and $p < 0.0001$, respectively.

(0.95 mm^2 ± 0.71).

Qualitative analysis was then performed to analyse the ability of scaffolds to induce vascularisation within the defect (Fig. 7I). The histological explants were graded from 1 to 3 regarding the presence of blood vessels, where 1 indicates a low population of blood vessels while score of 3 indicates a high and dense blood vessel population. All the histological samples from the miR-26a-scaffold condition scored 2 (50 % of the samples) and 3 (50 % of the samples), indicating the ability of the scaffold to enhance vasculogenesis compared to miR-free scaffolds ($p = 0.095$). The miR-free scaffold showed less developed blood vessel infiltration scoring 1 for 20 %, 2 for 65 % and 3 for 15 % of the samples. Collectively, the data indicated that miR-26 scaffold enhanced bone repair resulting in highly mineralised and vascularised tissue.

4. Discussion

The primary aim of this study was to develop a collagen-nanohydroxyapatite (coll-nHA) scaffold capable of delivering miRNA-26a-complexed RALA nanoparticles, with the goal of promoting both angiogenesis and osteogenesis for the accelerated repair of large bone defects. Initially, various formulations of miRNA-26a-RALA nanoparticles were screened using physicochemical methods to determine the optimal N:P ratio of 8, considering size, cargo, morphology, and stability. In 2D culture, hMSCs effectively internalised miRNA-26a nanoparticles, leading to enhanced production of ALP, an early osteogenic marker at day 7, and calcium deposition at day 14. Encouraged by the osteogenic potential of therapeutic miRNA-26a, the nanoparticles were successfully incorporated into osteogenic coll-nHA scaffolds. The miRNA-26a scaffolds demonstrated sustained release, retaining 70–90 % of the cargo for up to day 28 under static conditions and effectively transfected hMSCs *in vitro*. Consequently, there was an upregulated production of osteogenic (e.g., ALP) and angiogenic (e.g., VEGF) markers, indicative of the involvement of miRNA-26a in angiogenic-osteogenic coupling. Moving forward, the potential of the miRNA-26a scaffold was evaluated in critical-sized defects *in vivo* using male Wistar rats. The miRNA-26a activated scaffold exhibited superior bone tissue production within the defect site compared to miRNA-free scaffolds with known regenerative capacity. Additionally, histological and μCT data demonstrated enhanced mineralisation and vascularisation of newly formed tissue in the miRNA-26a scaffold group. In summary,

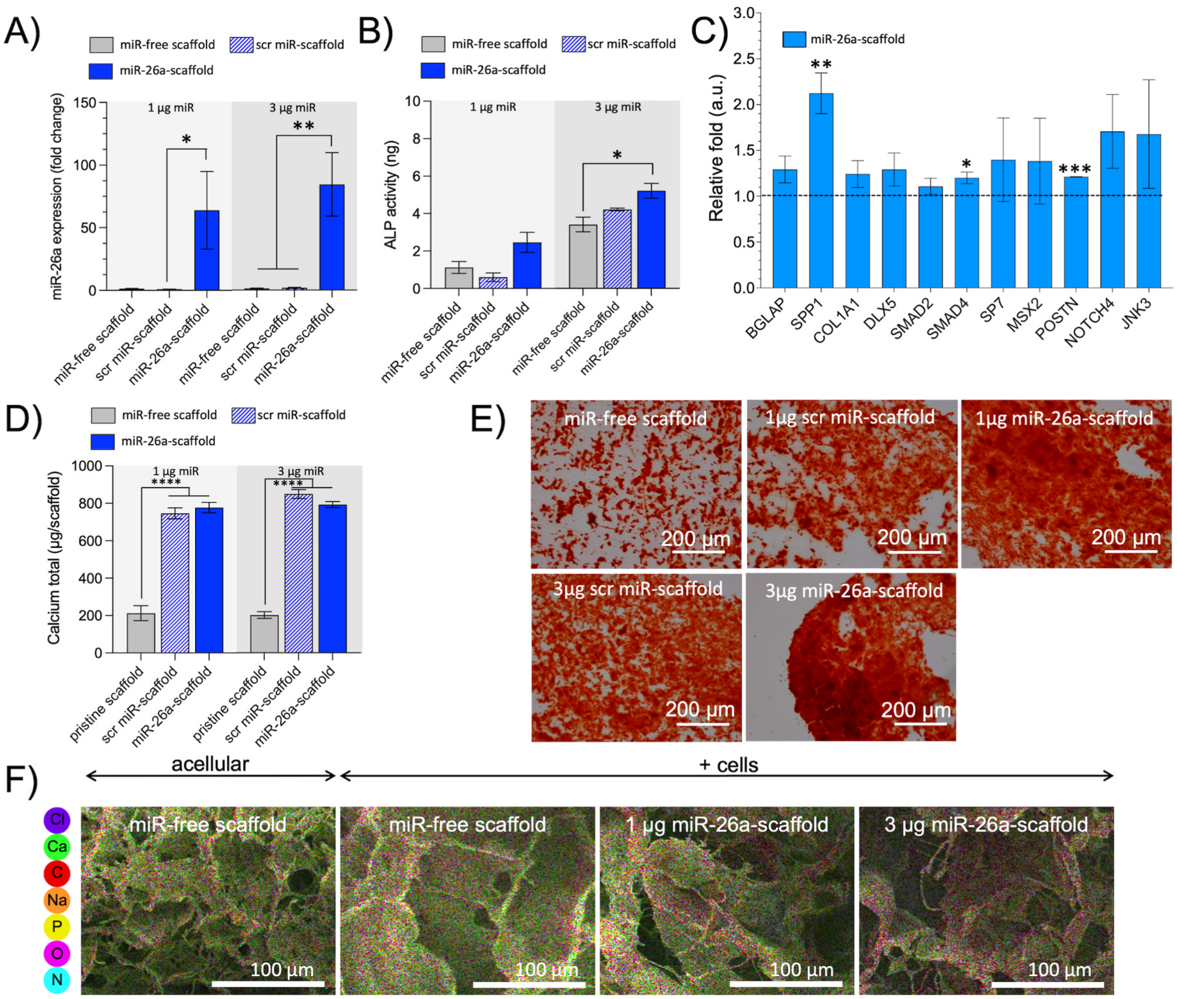

Fig. 5. miR-26a-activated scaffolds enhanced hMSC-mediated osteogenesis A) qPCR demonstrated significantly increased miR-26a levels in the miR-26a-activated scaffold at Day 3, indicating functional efficiency. **B)** miR-26a-activated scaffolds enhanced the secretion of ALP, an early marker of osteogenesis, **C)** enhanced expression of osteogenic markers and **D)** they stimulated calcium production. **E)** Alizarin red staining showed larger aggregates of calcium deposits in miR-activated scaffolds compared to miR-free scaffolds. **F)** The EDX data, performed on scaffolds subjected to 28 days of cell culture, presented calcium precipitates. *, **, and ****$p < 0.05$, $p < 0.01$, and $p < 0.0001$, respectively. The dashed black line on graph C indicates a threshold of 1. Pristine scaffolds refer to the scaffold which has not been exposed to cell culture media. (For interpretation of the references to color in this figure legend, the reader is referred to the Web version of this article.)

these results highlight that miRNA-26a-activated scaffolds can induce both angiogenic and osteogenic pathways *in vitro* and *in vivo*, showcasing the potential of this system as a novel therapy for healing large traumatic bone defects.

To ensure effective delivery to the cells, we determined the optimal amounts of miRNA-26a nanoparticles for hMSCs: 0.5 μg in monolayer 2D cell culture and 1 μg and 3 μg in coll-nHA scaffolds. Given the significance of spatiotemporal release in achieving controlled localised delivery at the implantation site, we investigated the release profiles of miRNA-26a from coll-nHA scaffolds. The scaffolds exhibited an initial burst release, releasing approximately 200–250 ng of genetic cargo within the first 24 h, followed by a slower diffusion-mediated release. Overall, the coll-nHA scaffolds retained 70–90 % of the cargo during the 28-day study period. These findings align with our previous observations, where we demonstrated that coll-nHA scaffolds retained approximately 80 % of recombinant bone morphogenetic protein [43]. While release profiles are influenced by multiple factors such as drug molecular weight, scaffold-cargo affinity, vector type, and scaffold loading capacity [44–46], among others, we hypothesise that the high retention observed may be attributed to the presence of hydroxyapatite in the scaffold. The presence of HA likely enhances the scaffold's capacity to adsorb and retain cargoes, ensuring prolonged retention beyond the initial release [47]. The initial burst release of miR-26a nanoparticles is associated with the fact that nanoparticles are not covalently attached to the surface, leading to the initial diffusion of miR-26a nanoparticles into the media within the first hours [48].

It is important to note that the concentrations of therapeutic miRNA used in this study did not exhibit cytotoxic effects on cells, as they fell within the optimal range (0.1–3 μg) reported in previous literature [49, 50]. Notably, the cells showed an increase in endogenous miR-26a levels, reaching over 2500-fold, 64-fold, and 84-fold for 2D culture, 1 μg loaded scaffold, and 3 μg loaded scaffold, respectively. The observed differences between 2D and 3D cell cultures could potentially be attributed to variations in the amount of miRNA delivered to the cells due to different miRNA-to-cell ratios. However, it is worth mentioning that there is considerable disparity in the literature regarding the correlation between the amount of miRNA delivered and its functionality. Previous studies investigating the delivery of miR-26a have reported inconsistent outcomes. For example, the delivery of 50 nmol of miR-26a combined with self-assembled polyplexes into osteoblastic cells resulted in a 3-fold increase [51]. In contrast, Zou et al. achieved over a 2500-fold increase in miR-26a levels in bone marrow-derived BMSCs when transfected with silica nanoparticles [52]. Yan et al. reported a >2500-fold expression of miR-26a in rat MSCs 24 h post-transfection

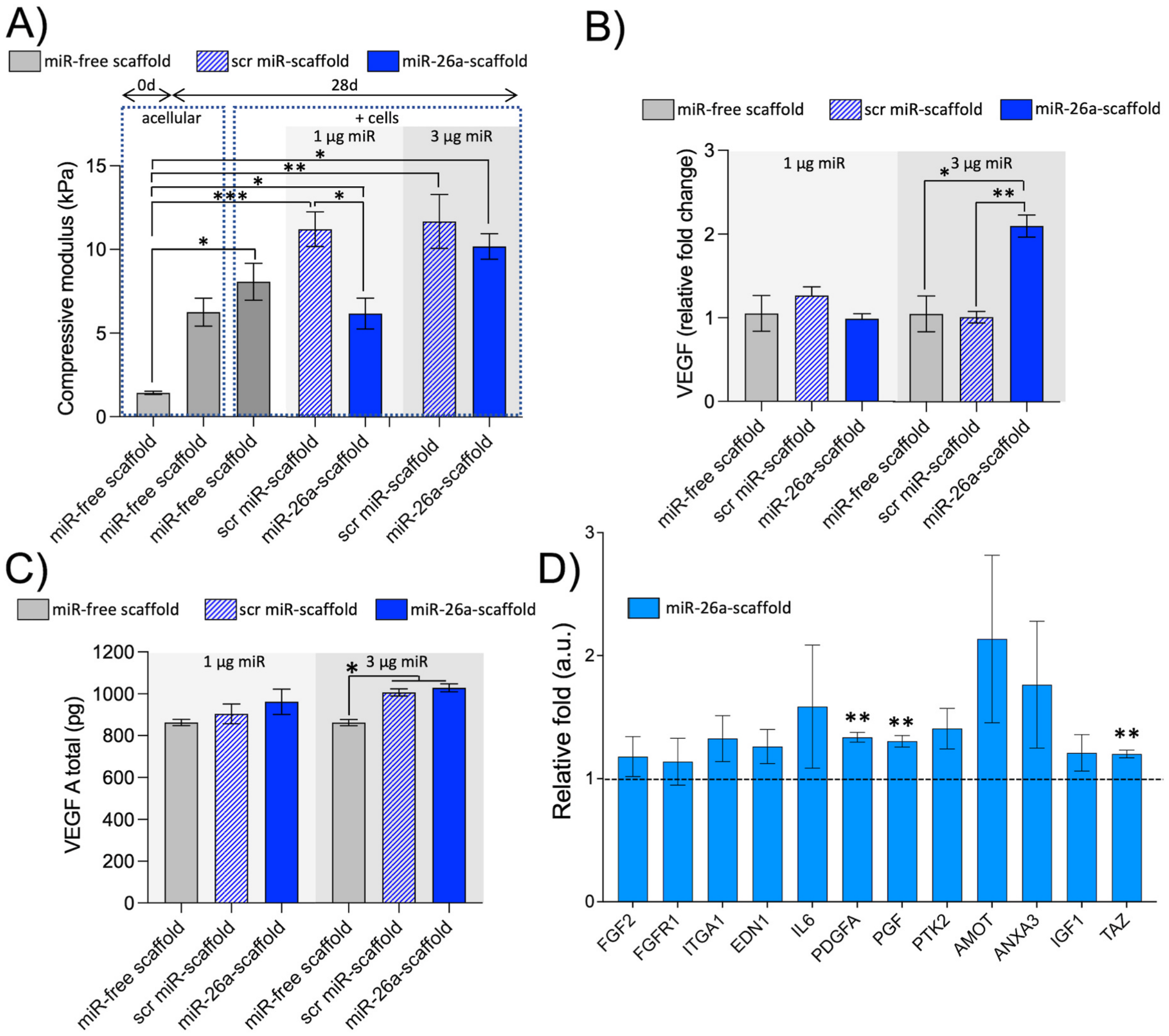

Fig. 6. miR-26a-activated scaffolds enhanced hMSC-mediated angiogenesis A) The scaffolds exposed to cell culture conditions showed greater compressive modulus compared to the pristine, miR-free scaffold. The hMSCs incubated with miR-26a-activated scaffold presented greater **B)** expression and **C)** secretion of vascular endothelial growth factor (VEGF), an indicator of angiogenesis. **D)** The culture of hMSCs on the miR-26-activated scaffold also enhanced the expression of genes involved in angiogenesis. *, **, ***, and **** correspond to $p < 0.05$, $p < 0.01$, $p < 0.001$, and $p < 0.0001$, respectively. The dashed blue lines on graph A indicate acellular groups and groups which were cultured with cells. 'The pristine scaffold' on graph A refers to the scaffold which wasn't subjected to cell culture conditions. The dashed black line on graph D indicates a threshold of 1. (For interpretation of the references to color in this figure legend, the reader is referred to the Web version of this article.)

with a non-viral system combining mesoporous silicon nanoparticles and KALA peptide, which delivered 20 μg of the cargo [24]. Taken together, our results demonstrate the effectiveness of both 2D and 3D systems in transfecting hMSC, which are known to be challenging primary cell types to transfect [53].

The successful transfection of hMSCs was reflected in enhanced osteogenesis *in vitro*, leading to increased production of ALP and mineralisation in both 2D and 3D systems. Additionally, miR-26a-activated scaffolds enhanced the expression of relevant osteogenic markers such as SPP1, SMAD4, and POSTN. These findings are consistent with previous studies. The enhanced expression of ALP and SPP1 was also reported by Yan et al., after transfecting rat MSCs with 20 μg of miR-26a nanoparticles [24]. The enhanced levels of SMAD4 and TAZ, an osteogenic and angiogenic factor, indicate that one of the possible mechanisms of miR-26a in stimulating osteogenesis is through affecting the SMAD4-TAZ axis. TAZ plays a pivotal role in osteogenesis by binding to SMAD4, co-activating transcription factors, which drive the osteoblastic differentiation programme of perichondrial mesenchymal stem cells (MSC) and suppress adipogenic differentiation [54,55]. The delivery of miR-26a also increased the levels of JNK3, which has been associated with bone repair. Our previous findings showed that scaffolds activated with JNK3 promote osteogenesis and angiogenesis, resulting in enhanced bone regeneration within just 4 weeks when implanted into rat calvarial defects [42]. Overall, the delivery of miR-26a positively influences osteogenesis by influencing a series of osteogenic pathways. For instance, Liu et al. demonstrated that the delivery of miR-26a into MSCs using a lentivirus vector doubled the number of ALP-positive cells at day 14 compared to the untransfected group [25]. Similarly, Li et al. showed that *in vitro* transfection of mouse and human BMSCs with 50 nM of miR-26a mimics resulted in a 2.4-fold and 10-fold increase in the expression of early-stage markers Runx2 and BMP2, respectively. Moreover, this translated to an 8.5-fold enhancement of the late-stage marker OCN in BMSCs, leading to increased ALP production and cell mineralisation [26]. Zou et al. demonstrated that miR-26a stimulates the viability and proliferation of osteoblasts and promotes osteogenesis [52]. Similarly, the osteogenic differentiation of BMSCs and transfected with miR-26a mimics was significantly augmented, as evidenced by increased calcium deposition and the expression levels of ALP and osteocalcin [56]. The present study investigates the pathways involved in miR-26a-induced osteogenesis in MSCs and its effects on

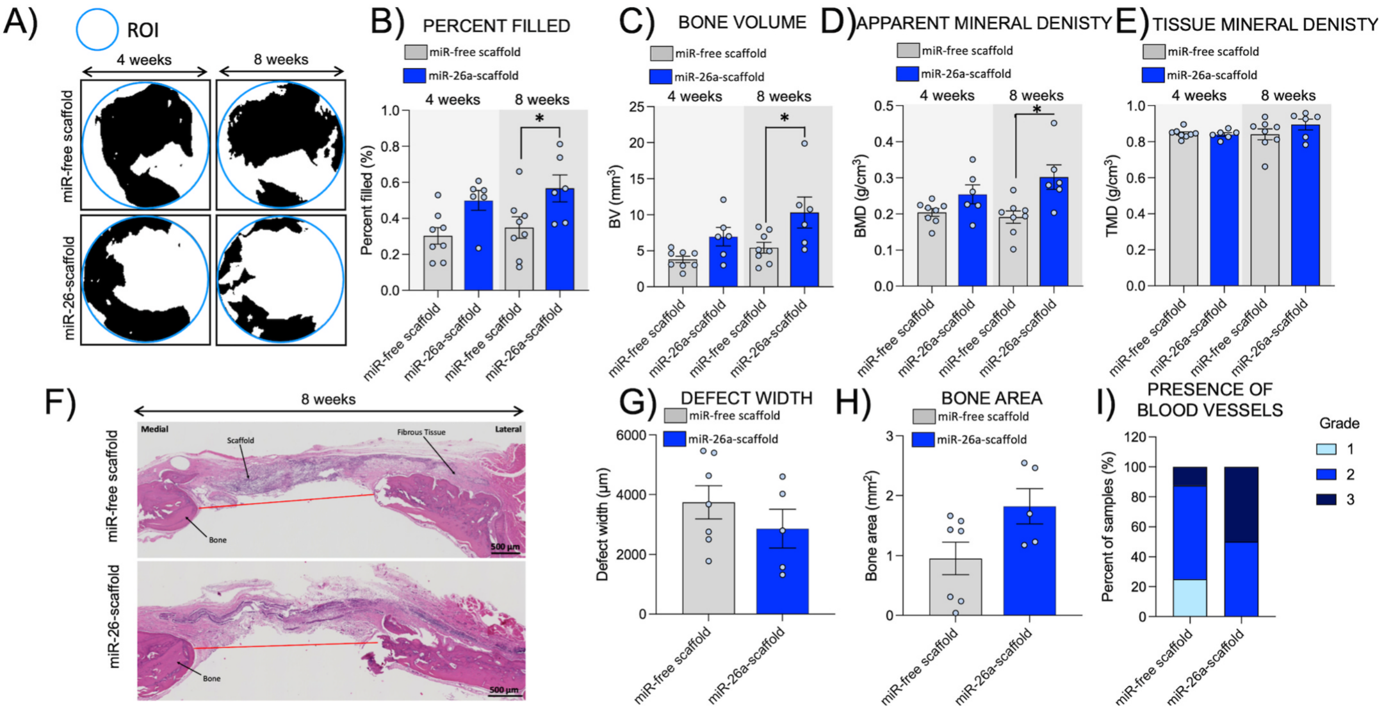

Fig. 7. Accelerated bone repair of miR-26a-activated scaffolds in critical-sized calvarial defects at week 4 and 8 post-implantation A) Representative micro CT reconstructions (left) of bone explants at weeks 4 and 8 for miR-free scaffold and miR-26a-activated scaffold. The blue circle represents the region of interest (ROI). The white area within the ROI indicates newly formed bone. **B)** Percentage filled, **C)** Bone volume, **D)** Apparent mineral density **E)** Tissue mineral density, **F)** Representative H&E scans at week 8 with marked scaffold, defect width, fibrous tissue and bone showed that miR-26a-activated scaffolds reduced **G)** defect width and increased **H)** bone area resulting in **I)** increased presence of blood vessels. *$p < 0.05$. (For interpretation of the references to color in this figure legend, the reader is referred to the Web version of this article.)

angiogenesis. We demonstrate that miR-26a promotes osteogenic differentiation in bone-derived MSCs primarily through the Wnt and BMP signalling pathways, while in adipose-derived MSCs, the SMAD1 pathway plays a predominant role [57–59]. Additionally, miR-26a targets CDK6 and HDAC4 proteins [60], further contributing to the osteogenic differentiation process. The intricate interplay between miR-26a and these signalling pathways highlights its potential as a therapeutic agent for promoting osteogenesis in MSCs.

We further investigated the effect of miR-26a on angiogenesis in MSCs and observed a context-dependent regulation. In our scaffold system, the delivery of miR-26a leads to enhanced production of VEGF, PDGFA, PGF, and TAZ in hMSCs, indicating the stimulation of angiogenesis. miR-26a has been previously shown to influence PDGFA as reported by Yang et al. [61]. The upregulation of PDGFA is particularly relevant in the context of bone regeneration as it positively influences angiogenesis and osteogenesis. This was previously reported by Zhang et al., demonstrating that MSCs transduced with PDGF isoforms activated the ERK1/2 signalling pathway, enhancing the migration and angiogenesis of vascular endothelial cells *in vitro* and promoting vascularisation in a critical-sized rat calvarial defect model [62]. The delivery of miR-26a also stimulated PGF, a member of the vascular endothelial growth factor (VEGF) family, which is a mechanosensitive gene with pro-angiogenic and pro-osteogenic roles [63]. Our previous research showed that the functionalisation of biomaterial scaffolds with PGF resulted in enhanced calcium deposition by human MSCs *in vitro*, which translated into enhanced calvarial defect healing *in vivo* [64]. Similarly, the activation of the YAP/TAZ pathway also promotes the formation of new blood vessels, and its upregulation through miR-26a indicates the strong involvement of this genetic cargo in angiogenesis [65]. Liu et al. showed that transfection of mouse and human bone marrow MSCs with miR-26a mimics resulted in increased expression of angiogenic markers, including VEGF and angiopoietin-1 (ANGP1) [26]. Moreover, Zuo et al. demonstrate the angiogenic potential of miR-26a by transfecting human umbilical vein endothelial cells with CD34$^+$ cell-derived exosomes containing miR-26a, which induces migration of endothelial cells and tube formation [66]. Multiple pathways have been implicated in miR-26a-induced angiogenesis, such as the hepatocyte growth factor-cMet pathway and the bone morphogenetic protein/-Smad1 pathway in conditions like hepatocellular carcinoma, acute myocardial infarction, and diabetes mellitus [67–69]. Furthermore, miR-26a has been shown to enhance angiogenesis in osseous defects or glioma by increasing the expression levels of hypoxia-inducible factor-1α (HIF-1α), VEGF, and Ang1 [26,70]. Our findings underscore the potential of miR-26a to enhance angiogenesis in bone regeneration, positioning it as a promising therapeutic candidate for the treatment of bone defects and disorders.

Angiogenic-osteogenic coupling is essential for bone repair, ensuring that newly formed bone is vascularised, thereby providing necessary nutrients for bone cells and facilitating further bone formation. Our miR-26a-activated scaffolds stimulated a myriad of genes which play dual roles in both angiogenesis and osteogenesis, including PDGFA, PGF, and TAZ. PDGFA is known to be secreted by preosteoclasts, and its pivotal role in angiogenic-osteogenic coupling consists of inducing migration of endothelial cells, stabilising newly formed vessels, and guiding cellular components for osteoblast differentiation [2]. Similarly, PGF contributes to the formation and maturation of blood vessels providing nutrients and osteoprogenitor cells to the bone formation sites, facilitating the process of osteogenesis [2,64]. TAZ and its paralog YAP (Yes-associated protein) are transcriptional co-activators in the Hippo signalling pathway that play significant roles in mechanotransduction, angiogenesis and stem cell differentiation. For example, Lee et al. showed that adipose stem cells (ASCs), transfected with BMP2-/VEGF, produce higher levels of TAZ, resulting in higher calcium deposition and increased angiogenesis *in vitro* [71]. Overall, our results underline the capacity of the miR-26a-activated scaffolds to induce bone formation through angiogenic-osteogenic coupling *in vitro*. However, one of the limitations of this work is that the data comes from *in vitro* evaluation. These results should be contrasted with a thorough *in vivo* evaluation to confirm specific pathways and genes impacted by miR-26a.

Having demonstrated the dual role of miR-26a *in vitro,* we proceeded to the final and most important aim of this study which focused on determining the ability of miR-26a-activated scaffolds to promote bone regeneration *in vivo*, specifically in a critical-sized calvarial defect model in rats. After 8 weeks, μCT analysis and histological evaluation revealed that the miR-26a-activated scaffolds significantly enhanced new bone formation, bone volume, and bone mineral density compared to the miR-free scaffolds. Additionally, histological analysis demonstrated a trend towards increased vascularisation within the defect site, indicating the ability of miR-26a-activated scaffolds to foster angiogenesis. These findings align with previous studies demonstrating the positive effects of miR-26a on bone regeneration in various animal models, including mice and rats. Researchers have reported increased bone volume, elevated expression of osteogenic markers (e.g., Runx2 and OC), and enhanced vascularisation as a result of microRNA-26a delivery using different scaffold systems [25,26,51]. The potential mechanism underlying the positive influence of miR-26a on angiogenic-osteogenic coupling may be attributed to its elevated expression in newly formed bones, which enhances vascular endothelial growth factor (VEGF) secretion. Bone, as a highly vascularised tissue, depends on well-coordinated angiogenic-osteogenic coupling for regeneration [26]. For instance, Zuo et al., evaluated the osteogenic capacity of microRNA-26a in an osteonecrotic femoral head model in female Sprague–Dawley (SD) rats demonstrating that the delivery of the cargo using exosomes enhances bone volume and trabeculae number. Moreover, the authors showed that the cargoes foster the vessel network and enhance the number of VEGF-stained cells Furthermore, it has been reported that miR-26a is involved in VEGF-mediated angiogenesis via the regulation of endothelial nitric oxide synthase activity. This regulation is modulated by the effect of miR-26a on the expression of NUS1 dehydrodolichyl diphosphate synthase subunit (NgBR) by directly targeting the NgBR 3′UTR. Overall, the results suggest that miR-26a-activated scaffolds possess significant potential in enhancing bone repair, leading to the formation of highly mineralised and vascularised tissue, which is crucial for effective bone regeneration *in vivo,* making this system extremely advantageous for bone.

5. Conclusions

Our study introduces an approach for treating critical-sized bone defects using cell-free miR-26a activated scaffolds, which have the potential to become a new 'off-the-shelf' product capable of stimulating bone healing through osteogenic-angiogenic coupling. The innovative combination of osteogenic coll-nHA scaffolds with a microRNA therapeutic that induces dual pathways targeting the two most relevant processes in bone regeneration is a significant advancement in the field of tissue engineering and regenerative medicine. The microRNA-activated scaffold system acts as a carrier system that enables localised delivery, ensuring lower doses and administration frequency while enhancing efficacy and reducing aberrant effects. Furthermore, the effective delivery of miRNAs from biomaterial scaffolds also demonstrates their feasibility as a platform to carry therapeutic nucleic acids and small molecules, opening the door to a myriad of tissue engineering applications beyond bone repair.

Author contribution

Joanna M. Sadowska: Conceptualization, Formal analysis, Investigation, Writing - Original Draft, Funding acquisition; **Monika Ziminska**: Conceptualization, Formal analysis, Investigation, Writing - Original Draft; **Cole Ferreira**: Conceptualization, Formal analysis, Investigation, Writing - Original Draft; **Austyn Matheson**: Writing - Review & Editing; **Auden Balouch**: Formal analysis, Investigation, Writing - Review & Editing; **Jasmine Bogle**: Formal analysis, Investigation; **Samantha Wojda**: Conceptualization, Writing - Review & Editing; **John Redmond**: Formal analysis, Investigation; **Ahmed Elkashif**: Formal analysis, Writing - Review & Editing; **Nicholas Dunne**: Conceptualization, Writing - Review & Editing, Supervision, Funding acquisition; **Helen O. McCarthy**: Conceptualization, Writing - Review & Editing, Supervision, Funding acquisition; **Seth Donahue**: Conceptualization, Writing - Review & Editing, Supervision, Funding acquisition; **Fergal J. O'Brien**: Conceptualization, Writing - Review & Editing, Supervision, Funding acquisition.

Declaration of competing interest

The authors declare the following financial interests/personal relationships which may be considered as potential competing interests: Fergal O'Brien reports financial support was provided by Science Foundation Ireland. Fergal O'Brien reports financial support was provided by European Research Council. Joanna Sadowska reports financial support was provided by European Commission. Joanna Sadowska reports financial support was provided by ON Foundation. Seth Donahue reports financial support was provided by National Science Foundation. Helen O. McCarthy reports financial support was provided by Science Foundation Ireland. Helen O. McCarthy has patent #WO2014087023 issued to Helen O. McCarthy.

Data availability

Data will be made available on request.

Acknowledgements

The authors acknowledge funding from National Science Foundation (Award # 1854387) and Science Foundation Ireland under the US-Ireland Research and Development Partnership (17/ US/3437; Ireland). FJOB acknowledges funding from the European Research Council under the European Community's Horizon 2020 research and innovation programme under the ERC Advanced Grant agreement n° 788753 (ReCaP). JMS benefits from a Marie Skłodowska-Curie Individual Fellowships from the European Commission through the H2020 project GAMBBa (Project ID: 892389). The project (21–053) was supported by a grant from the ON Foundation, Switzerland. HM acknowledges US-Ireland Grant 130. We thank Evan Dempsey and Paige Ruschke for help with animal handling and surgical procedures, and Aladdin Mohammed for assistance with analysing the micro-computed tomography scans.

Appendix A. Supplementary data

Supplementary data to this article can be found online at https://doi.org/10.1016/j.biomaterials.2023.122398.

References

[1] J.M. Kanczler, R.O.C. Oreffo, Osteogenesis and angiogenesis: the potential for engineering bone, Eur. Cells Mater. 15 (May 2014) (2008) 100–114, https://doi.org/10.22203/eCM.v015a08.

[2] A. Grosso, M.G. Burger, A. Lunger, D.J. Schaefer, A. Banfi, N. Di Maggio, It takes two to tango: coupling of angiogenesis and osteogenesis for bone regeneration, Front. Bioeng. Biotechnol. 5 (NOV) (2017) 1–7, https://doi.org/10.3389/fbioe.2017.00068.

[3] M.K. Sen, T. Miclau, Autologous iliac crest bone graft: should it still be the gold standard for treating nonunions? Injury 38 (SUPPL. 1) (2007) 2–7, https://doi.org/10.1016/j.injury.2007.02.012.

[4] S.P. Cowley, L.D. Anderson, Hernias through donor sites for iliac-bone grafts, J. Bone Joint Surg. Am. 65 (7) (Sep. 1983) 1023–1025 [Online]. Available: http://www.ncbi.nlm.nih.gov/pubmed/6885861.

[5] G.L. Koons, M. Diba, A.G. Mikos, Materials design for bone-tissue engineering, Nat. Rev. Mater. 5 (8) (2020) 584–603, https://doi.org/10.1038/s41578-020-0204-2.

[6] T.M. De Witte, L.E. Fratila-Apachitei, A.A. Zadpoor, N.A. Peppas, Bone tissue engineering via growth factor delivery: from scaffolds to complex matrices, Regen. Biomater. 5 (4) (2018) 197–211, https://doi.org/10.1093/rb/rby013.

[7] E.A. Bayer, R. Gottardi, M.V. Fedorchak, S.R. Little, The scope and sequence of growth factor delivery for vascularized bone tissue regeneration, J. Control. Release 219 (2015) 129–140, https://doi.org/10.1016/j.jconrel.2015.08.004.

[8] Y. Wang, M.R. Newman, D.S.W. Benoit, Development of controlled drug delivery systems for bone fracture-targeted therapeutic delivery: a review, Eur. J. Pharm. Biopharm. 127 (1) (Jun. 2018) 223–236, https://doi.org/10.1016/j.ejpb.2018.02.023.

[9] M.M. Martino, P.S. Briquez, K. Maruyama, J.A. Hubbell, Extracellular matrix-inspired growth factor delivery systems for bone regeneration, Adv. Drug Deliv. Rev. 94 (Nov. 2015) 41–52, https://doi.org/10.1016/j.addr.2015.04.007.

[10] W.J. King, P.H. Krebsbach, Growth factor delivery: how surface interactions modulate release in vitro and in vivo, Adv. Drug Deliv. Rev. 64 (12) (Sep. 2012) 1239–1256, https://doi.org/10.1016/j.addr.2012.03.004.

[11] I.M. Castaño, R.M. Raftery, C.M. Curtin, J. Grillari, H. Redl, F.J. O’Brien, microRNA Modulation, in: Cell Engineering and Regeneration, Springer International Publishing, Cham, 2019, pp. 1–66.

[12] E.A. Clark, S. Kalomoiris, J.A. Nolta, F.A. Fierro, Concise review: MicroRNA function in multipotent mesenchymal stromal cells, Stem Cell. 32 (5) (2014) 1074–1082, https://doi.org/10.1002/stem.1623.

[13] N. Bushati, S.M. Cohen, MicroRNA functions, Annu. Rev. Cell Dev. Biol. 23 (2007) 175–205, https://doi.org/10.1146/annurev.cellbio.23.090506.123406.

[14] A.W. James, et al., A review of the clinical side effects of bone morphogenetic protein-2, Tissue Eng. - Part B Rev. 22 (4) (2016) 284–297, https://doi.org/10.1089/ten.teb.2015.0357.

[15] A. Oryan, A. Alidadi, A. Moshiri, A. Bigham-Sadegh, Bone morphogenetic proteins: a powerful osteoinductive compound with non-negligible side effects and limitations, Biofactors 40 (5) (2014) 459–481, https://doi.org/10.1002/biof.1177.

[16] I. Mencía Castaño, C.M. Curtin, G.P. Duffy, F.J. O’Brien, Next generation bone tissue engineering: non-viral miR-133a inhibition using collagen-nanohydroxyapatite scaffolds rapidly enhances osteogenesis, Sci. Rep. 6 (1) (Sep. 2016), 27941, https://doi.org/10.1038/srep27941.

[17] I. Mencía Castaño, C.M. Curtin, G.P. Duffy, F.J. O’Brien, Harnessing an inhibitory role of miR-16 in osteogenesis by human mesenchymal stem cells for advanced scaffold-based bone tissue engineering, Tissue Eng. Part A 25 (1–2) (Jan. 2019) 24–33, https://doi.org/10.1089/ten.tea.2017.0460.

[18] G. Wu, et al., In situ controlled release of stromal cell-derived factor-1α and antimiR-138 for on-demand cranial bone regeneration, Carbohydr. Polym. 182 (Feb. 2018) 215–224, https://doi.org/10.1016/j.carbpol.2017.10.090.

[19] S. Wang, et al., The endothelial-specific MicroRNA miR-126 governs vascular integrity and angiogenesis, Dev. Cell 15 (2) (Aug. 2008) 261–271, https://doi.org/10.1016/j.devcel.2008.07.002.

[20] P. Fasanaro, et al., MicroRNA-210 modulates endothelial cell response to hypoxia and inhibits the receptor tyrosine kinase ligand ephrin-A3, J. Biol. Chem. 283 (23) (2008) 15878–15883, https://doi.org/10.1074/jbc.M800731200.

[21] L. Poliseno, et al., MicroRNAs modulate the angiogenic properties of HUVECs, Blood 108 (9) (2006) 3068–3071, https://doi.org/10.1182/blood-2006-01-012369.

[22] X. Zhang, Y. Li, Y.E. Chen, J. Chen, P.X. Ma, Cell-free 3D scaffold with two-stage delivery of miRNA-26a to regenerate critical-sized bone defects, Nat. Commun. 7 (2016), https://doi.org/10.1038/ncomms10376.

[23] Z. Wang, et al., MicroRNA-26a-modified adipose-derived stem cells incorporated with a porous hydroxyapatite scaffold improve the repair of bone defects, Mol. Med. Rep. 12 (3) (2015) 3345–3350, https://doi.org/10.3892/mmr.2015.3795.

[24] J. Yan, et al., Effects of mir-26a on osteogenic differentiation of bone marrow mesenchymal stem cells by a mesoporous silica nanoparticle - PEI - peptide system, Int. J. Nanomed. 15 (2020) 497–511, https://doi.org/10.2147/IJN.S228797.

[25] Z. Liu, et al., Lentivirus-mediated microRNA-26a overexpression in bone mesenchymal stem cells facilitates bone regeneration in bone defects of calvaria in mice, Mol. Med. Rep. 18 (6) (2018) 5317–5326, https://doi.org/10.3892/mmr.2018.9596.

[26] Y. Li, et al., The promotion of bone regeneration through positive regulation of angiogenic-osteogenic coupling using microRNA-26a, Biomaterials 34 (21) (2013) 5048–5058, https://doi.org/10.1016/j.biomaterials.2013.03.052.

[27] Y. Li, et al., MiR-26a rescues bone regeneration deficiency of mesenchymal stem cells derived from osteoporotic mice, Mol. Ther. 23 (8) (2015) 1349–1357, https://doi.org/10.1038/mt.2015.101.

[28] K. Kim, et al., MicroRNA-26a regulates RANKL-induced osteoclast formation, Mol. Cell. 38 (1) (2014) 75–80, https://doi.org/10.14348/molcells.2015.2241.

[29] R.N. Power, B.L. Cavanagh, J.E. Dixon, C.M. Curtin, F.J. O’Brien, Development of a gene-activated scaffold incorporating multifunctional cell-penetrating peptides for pSDF-1α delivery for enhanced angiogenesis in tissue engineering applications, Int. J. Mol. Sci. 23 (3) (2022), https://doi.org/10.3390/ijms23031460.

[30] A.J. Ryan, J.P. Gleeson, A. Matsiko, E.M. Thompson, F.J. O’Brien, Effect of different hydroxyapatite incorporation methods on the structural and biological properties of porous collagen scaffolds for bone repair, J. Anat. 227 (6) (2015) 732–745, https://doi.org/10.1111/joa.12262.

[31] F. David, et al., Enhanced bone healing using collagen-hydroxyapatite scaffold implantation in the treatment of a large multiloculated mandibular aneurysmal bone cyst in a thoroughbred filly, J. Tissue Eng. Regen. Med. 9 (10) (Oct. 2015) 1193–1199, https://doi.org/10.1002/term.2006.

[32] C.M. Curtin, et al., Innovative collagen nano-hydroxyapatite scaffolds offer a highly efficient non-viral gene delivery platform for stem cell-mediated bone formation, Adv. Mater. 24 (6) (2012) 749–754, https://doi.org/10.1002/adma.201103828.

[33] R.M. Raftery, et al., Delivery of the improved BMP-2-Advanced plasmid DNA within a gene-activated scaffold accelerates mesenchymal stem cell osteogenesis and critical size defect repair, J. Control. Release 283 (2018) 20–31, https://doi.org/10.1016/j.jconrel.2018.05.022.

[34] R.M. Raftery, et al., Translating the role of osteogenic-angiogenic coupling in bone formation: highly efficient chitosan-pDNA activated scaffolds can accelerate bone regeneration in critical-sized bone defects, Biomaterials 149 (2017) 116–127, https://doi.org/10.1016/j.biomaterials.2017.09.036.

[35] H.O. McCarthy, et al., Development and characterization of self-assembling nanoparticles using a bio-inspired amphipathic peptide for gene delivery, J. Control. Release 189 (Sep. 2014) 141–149, https://doi.org/10.1016/j.jconrel.2014.06.048.

[36] L.P. Yan, et al., Collagen/GAG scaffolds activated by RALA-siMMP-9 complexes with potential for improved diabetic foot ulcer healing, Mater. Sci. Eng. C 114 (January) (2020), 111022, https://doi.org/10.1016/j.msec.2020.111022.

[37] C.M. McCrudden, et al., Gene therapy with RALA/iNOS composite nanoparticles significantly enhances survival in a model of metastatic prostate cancer, Cancer Nanotechnol. 9 (1) (Dec. 2018) 5, https://doi.org/10.1186/s12645-018-0040-x.

[38] J. McCaffrey, et al., Transcending epithelial and intracellular biological barriers; a prototype DNA delivery device, J. Control. Release 226 (Mar. 2016) 238–247, https://doi.org/10.1016/j.jconrel.2016.02.023.

[39] E.M. McErlean, et al., Rational design and characterisation of an amphipathic cell penetrating peptide for non-viral gene delivery, Int. J. Pharm. 596 (Mar. 2021), https://doi.org/10.1016/J.IJPHARM.2021.120223.

[40] I.M. Castaño, et al., Rapid bone repair with the recruitment of CD206+M2-like macrophages using non-viral scaffold-mediated miR-133a inhibition of host cells, Acta Biomater. 109 (Jun. 2020) 267–279, https://doi.org/10.1016/j.actbio.2020.03.042.

[41] D.P. Walsh, R.M. Raftery, G. Chen, A. Heise, F.J. O’Brien, S. Cryan, Rapid healing of a critical-sized bone defect using a collagen-hydroxyapatite scaffold to facilitate low dose, combinatorial growth factor delivery, J. Tissue Eng. Regen. Med. 13 (10) (Oct. 2019) 1843–1853, https://doi.org/10.1002/term.2934.

[42] A. González-Vazquez, R.M. Raftery, S. Günbay, G. Chen, D.J. Murray, F.J. O’Brien, Accelerating bone healing in vivo by harnessing the age-altered activation of c-Jun N-terminal kinase 3, Biomaterials 268 (Jan. 2021), 120540, https://doi.org/10.1016/j.biomaterials.2020.120540.

[43] W.A. Lackington, et al., Incorporation of hydroxyapatite into collagen scaffolds enhances the therapeutic efficacy of rhBMP-2 in a weight-bearing femoral defect model, Mater. Today Commun. 29 (June) (2021), https://doi.org/10.1016/j.mtcomm.2021.102933.

[44] W.R. Gombotz, S.F. Wee, Protein release from alginate matrices, Adv. Drug Deliv. Rev. 31 (3) (1998) 267–285, https://doi.org/10.1016/S0169-409X(97)00124-5.

[45] W.N. Sivak, J. Zhang, S. Petoud, E.J. Beckman, Simultaneous drug release at different rates from biodegradable polyurethane foams, Acta Biomater. 5 (7) (2009) 2398–2408, https://doi.org/10.1016/j.actbio.2009.03.036.

[46] L. Ge, X. Tan, R. Sheng, J. Xiao, Layer-by-layer self-assembly of giant polyelectrolyte microcapsules templated by microbubbles as potential hydrophilic or hydrophobic drug delivery system, Colloids Interface Sci. Commun. 47 (2022), 100603, https://doi.org/10.1016/j.colcom.2022.100603.

[47] M. Imranul Alam, I. Asahina, K. Ohmamiuda, K. Takahashi, S. Yokota, S. Enomoto, Evaluation of ceramics composed of different hydroxyapatite to tricalcium phosphate ratios as carriers for rhBMP-2, Biomaterials 22 (12) (2001) 1643–1651, https://doi.org/10.1016/S0142-9612(00)00322-7.

[48] R. Jamaledin, et al., Engineered microneedle patches for controlled release of active compounds: recent advances in release profile tuning, Adv. Ther. 3 (12) (Dec. 2020), https://doi.org/10.1002/adtp.202000171.

[49] K.A. Fitzgerald, et al., Nanoparticle-mediated siRNA delivery assessed in a 3D co-culture model simulating prostate cancer bone metastasis, Int. J. Pharm. 511 (2) (2016) 1058–1069, https://doi.org/10.1016/j.ijpharm.2016.07.079.

[50] L.S. Costard, et al., Layered double hydroxide as a potent non-viral vector for nucleic acid delivery using gene-activated scaffolds for tissue regeneration applications, Pharmaceutics 12 (12) (2020) 1–24, https://doi.org/10.3390/pharmaceutics12121219.

[51] X. Zhang, Y. Li, Y.E. Chen, J. Chen, P.X. Ma, Cell-free 3D scaffold with two-stage delivery of miRNA-26a to regenerate critical-sized bone defects, Nat. Commun. 7 (2016) 1–15, https://doi.org/10.1038/ncomms10376.

[52] J. Zou, et al., The regulatory roles of miR-26a in the development of fracture and osteoblasts, Ann. Transl. Med. 10 (2) (2022) 37, https://doi.org/10.21037/atm-21-6101, 37.

[53] O. Gresch, L. Altrogge, Transfection of difficult-to-transfect primary mammalian cells, Methods Mol. Biol. 801 (4) (2012) 65–74, https://doi.org/10.1007/978-1-61779-352-3_5.

[54] H. Kovar, L. Bierbaumer, B. Radic-sarikas, The YAP/TAZ pathway in osteogenesis and bone, Cells 9 (972) (2020) 1–34.

[55] J.S. Park, et al., A reciprocal role of the smad4-taz Axis in osteogenesis and adipogenesis of mesenchymal stem cells, Stem Cell. 37 (3) (2019) 368–381, https://doi.org/10.1002/stem.2949.

[56] L. Sun, et al., MiR-26a promotes fracture healing of nonunion rats possibly by targeting SOSTDC1 and further activating Wnt/β-catenin signaling pathway, Mol. Cell. Biochem. 460 (1–2) (2019) 165–173, https://doi.org/10.1007/s11010-019-03578-9.

[57] S. Li, et al., Effect of miR-26a-5p on the Wnt/Ca2+ pathway and osteogenic differentiation of mouse adipose-derived mesenchymal stem cells, Calcif. Tissue Int. 99 (2) (Aug. 2016) 174–186, https://doi.org/10.1007/s00223-016-0137-3.

[58] X. Su, et al., MiR-26a Functions Oppositely in Osteogenic Differentiation of BMSCs and ADSCs Depending on Distinct Activation and Roles of Wnt and BMP Signaling Pathway, 2015, https://doi.org/10.1038/cddis.2015.221.

[59] Z. Wang, et al., A regulatory loop containing miR-26a, GSK3β and C/EBPα regulates the osteogenesis of human adipose-derived mesenchymal stem cells, Sci. Rep. 5 (1) (Oct. 2015) 1–18, https://doi.org/10.1038/srep15280.

[60] H.-I. Trompeter, et al., MicroRNAs miR-26a, miR-26b, and miR-29b Accelerate Osteogenic Differentiation of Unrestricted Somatic Stem Cells from Human Cord Blood, 2013, https://doi.org/10.1186/1471-2164-14-111.

[61] X. Yang, et al., MiR-26a contributes to the PDGF-BB-induced phenotypic switch of vascular smooth muscle cells by suppressing Smad1, Oncotarget 8 (44) (2017) 75844–75853, https://doi.org/10.18632/oncotarget.17998.

[62] M. Zhang, et al., The effects of platelet-derived growth factor-BB on bone marrow stromal cell-mediated vascularized bone regeneration, Stem Cell. Int. 2018 (2018), 3272098, https://doi.org/10.1155/2018/3272098.

[63] R.J. McCoy, et al., Orchestrating osteogenic differentiation of mesenchymal stem cells - identification of placental growth factor as a mechanosensitive gene with a pro-osteogenic role, Stem Cell. 31 (11) (2013) 2420–2431, https://doi.org/10.1002/stem.1482.

[64] E.J. Sheehy, et al., Mechanobiology-informed regenerative medicine: dose-controlled release of placental growth factor from a functionalized collagen-based scaffold promotes angiogenesis and accelerates bone defect healing, J. Control. Release 334 (March) (2021) 96–105, https://doi.org/10.1016/j.jconrel.2021.03.031.

[65] A. Hooglugt, M.M. van der Stoel, R.A. Boon, S. Huveneers, Endothelial YAP/TAZ signaling in angiogenesis and tumor vasculature, Front. Oncol. 10 (February) (2021) 1–22, https://doi.org/10.3389/fonc.2020.612802.

[66] R. Zuo et al., "Exosomes Derived from Human CD34 + Stem Cells Transfected with miR-26a Prevent Glucocorticoid-Induced Osteonecrosis of the Femoral Head by Promoting Angiogenesis and Osteogenesis," doi: 10.1186/s13287-019-1426-3..

[67] B. Icli, et al., MicroRNA-26a regulates pathological and physiological angiogenesis by targeting BMP/SMAD1 signaling, Circ. Res. 113 (11) (Nov. 2013) 1231–1241, https://doi.org/10.1161/CIRCRESAHA.113.301780.

[68] X. Yang, et al., MicroRNA-26a suppresses angiogenesis in human hepatocellular carcinoma by targeting hepatocyte growth factor-cMet pathway, Hepatology 59 (5) (May 2014) 1874–1885, https://doi.org/10.1002/hep.26941.

[69] B. Icli, et al., Regulation of impaired angiogenesis in diabetic dermal wound healing by microRNA-26a, J. Mol. Cell. Cardiol. 91 (2016) 151–159, https://doi.org/10.1016/j.yjmcc.2016.01.007.

[70] X. Qian, et al., MicroRNA-26a promotes tumor growth and angiogenesis in glioma by directly targeting prohibitin, CNS Neurosci. Ther. 19 (10) (2013) 804–812, https://doi.org/10.1111/cns.12149.

[71] E. Lee, J.Y. Ko, J. Kim, J.W. Park, S. Lee, G. Il Im, Osteogenesis and angiogenesis are simultaneously enhanced in BMP2-/VEGF-transfected adipose stem cells through activation of the YAP/TAZ signaling pathway, Biomater. Sci. 7 (11) (2019) 4588–4602, https://doi.org/10.1039/c9bm01037h.